Dispersion in spatially-periodic chromatography media

by

Jesse J. Kirchner

Submitted to the Department of Mechanical Engineering
in partial fulfillment of the requirements for the degree of

Master of Science

at the

UNIVERSITY OF MICHIGAN

June 2003

Accepted by

Ernest F. Hasselbrink, Assistant Professor of Mechanical Engineering

William W. Schultz, Professor of Mechanical Engineering

Dispersion in spatially-periodic chromatography media

by

Jesse J. Kirchner

Submitted to the Department of Mechanical Engineering
on 20 June 2003, in partial fulfillment of the
requirements for the degree of
Master of Science

Abstract

Hydrodynamic dispersion in liquid chromatography devices leads to a decrease in resolution, implying increased separation time and thus increased cost. Microfabrication technology has recently eliminated or reduced other sources of band-broadening, but the use of spatially-periodic geometries for increased mass-transfer to surfaces in microfluidic chromatography columns leads to increased dispersion due to transverse velocity gradients. This thesis aims to simulate electrokinetically-driven hydrodynamic dispersion in a variety of two-dimensional spatially-periodic geometries (post arrays and capillaries) in the thin Debye-layer (TDL) limit. Potential flow fields were calculated in a periodic domain using both an inverse method and a Schwarz-Christoffel transform. A particle tracking method was used to model transport in (ϕ, ψ)-space. Convection was modelled as deterministic steps along a line of constant-ψ and a split-step Monte Carlo method was used to model diffusion. Long-time longitudinal dispersion D_L was calculated from the variance of the particle distribution versus time at many values of the Péclet number based on mean velocity potential, channel height, and binary diffusion coefficient. Functional fits with one or two free parameters for D_L versus Pe were chosen based on the literature. Best-fit parameters were found using a maximum likelihood method and correlated against different non-dimensional scales. The scale $(1 - \Lambda)$, a measure of the pore size, provides an excellent collapse of these fit parameters leading to general relations for longitudinal dispersion.

Thesis Supervisor: Ernest F. Hasselbrink
Title: Assistant Professor of Mechanical Engineering

Acknowledgments

I've had the pleasure of working with (as well as being advised by) Prof. Charlie Hasselbrink. Thanks to Prof. Bill Schultz for discussion of numerical methods and perturbation theory and also for intruducing me to amphibian libations in Indiana. I was introduced to numerical methods by Profs. Robert Krasny and Hans Johnston in the Mathematics Department at the University of Michigan and I'd like to specifically thank Prof. Krasny for suggesting the block-Thomas algorithm for solving block-tridiagonal systems. Thanks to Prof. Tobin Driscoll at the University of Delaware for creating Schwarz-Christoffel Toolbox for MATLAB and also for being kind enough to answer my emails.

In the summer of 2002, I was an intern at Sandia National Laboratories in Livermore, California supported by the Advanced Computing Research Institute. I'd like to thank Manager Mark Hoerstmeyer for material support. Thanks to my supervisor Mike Kanouff for discussion of numerical methods and making sure I was well taken care of. At Sandia, I had the opportunity to work with Stewart Griffiths. Stewart knows everything about everything and specifically, it was his work that inspired the use of the inverse method to perform our Monte Carlo simulations in (ϕ, ψ)-space. Finally, my cubical-mates Jeromy Hollinshead, Mark Pavol, and Serge Tchikanda as well as Anne Gutmann and Tammy Nguyen were a tremendous source of discussion and distraction.

At the 2002 APS Division of Fluid Dynamics meeting in Dallas, Texas, I had the good fortune to meet Profs. Andrew Bernoff from Harvey Mudd College and Lou Rossi from the University of Delaware. Thanks to Prof. Bernoff for suggesting a split-step scheme for simulating diffusion and convincing me that random numbers really are needed to model diffusion processes. Thanks to Prof. Rossi for discussing many alternative methods for simulating dispersion.

Thanks to my lab-mates here in Ann Arbor: Sneha Madhevan-Reese, Jung-Yim Min, Pat Hunt, Sun Min Kim, Taesung Kim, and Meng-Ping Chang.

Finally, thanks to all the people who have put up with me these past two years: Sylvia González, Connie Pagedas, Juan Francisco Reyes-Luna, Chris Walker, Christophe Gibaud, Charlie Funk, Alan McGaughey, and Chad Jagmin.

I would also like to thank the College of Engineering at the University of Michigan for support through the Regent's Fellowship and the US Department of Energy/Sandia National Laboratories for support through Doc. #23415.

Contents

List of Figures

List of Tables

Chapter 0

Notation

Operators

$\boldsymbol{\nabla}(\bullet)$	two-dimensional gradient operator in physical space
$\boldsymbol{\nabla} \cdot (\bullet)$	two-dimensional divergence operator in physical space
$\boldsymbol{\nabla} \times (\bullet)$	two-dimensional curl operator in physical space
$\Delta^{xy}(\bullet)$	two-dimensional Laplacian operator in physical space
$\Delta^{\phi\psi}(\bullet)$	two-dimensional Laplacian operator in inverse space
$(\bullet)_{\text{in}}$	value at inlet of periodic domain
$(\bullet)_{\text{out}}$	value at outlet of periodic domain
$(\bullet)_{\text{top}}$	value at top of periodic domain
$(\bullet)_{\text{bot}}$	value at bottom of periodic domain
$\overline{(\bullet)}$	spatial average
$(\bullet)_{jl}$	finite difference representation
$O[\bullet]$	order

Greek letters

α	constant in dispersion relation for unidirectional flow
α_k	Schwarz-Christoffel interior angles
α_1	parameter in first fit function
α_2	parameter in second fit function
$\alpha_{3,1}$	parameter in third fit function
$\alpha_{3,2}$	parameter in third fit function
Δ_{ij}	distance between i^{th} and j^{th} species distributions
δ_i	width of i^{th} species distribution
$\delta_{0,i}$	initial width of i^{th} species distribution
θ_{xy}	direction of spatial diffusion step

$\theta_{\phi\psi}$	direction of inverse diffusion step
Λ	non-dimensional pore size
λ	domain width
μ	mean of solute distribution
μ_{EO}	electroosmotic mobility
$\mu_{EP,i}$	electrophoretic mobility of i^{th} species
ν	kinematic viscosity
ρ	fluid density
σ	standard deviation
σ^2	variance of solute distribution
σ_{σ^2}	error on variance
$\sigma_{D^*_{L,i}}$	error on simulation value of normalized longitudinal disperion coefficient
Φ	electric potential
ϕ	velocity potential
$\phi(z)$	real part of complex function
(ϕ, ψ)	inverse space coordinates
$\delta\phi$	inverse step along streamline
χ^2	goodness of fit
χ^2_1	goodness of fit for first fit function
χ^2_2	goodness of fit for second fit function
χ^2_3	goodness of fit for third fit function
$\boldsymbol{\psi}$	stream function vector
ψ	stream function
$\psi(z)$	imaginary part of complex function
Ω	periodic domain
$\delta\Omega$	boundary of periodic domain
Ω'	periodic domain in inverse space
$\boldsymbol{\omega}$	vorticity vector

Others variables

$\boldsymbol{A}_i, \boldsymbol{B}_i, \boldsymbol{C}_i$	non-zero blocks of tridiagonal difference matrix
A	area of domain
a, b, c	example constants for finite difference matrix
a	particle radius
B	Brenner scalar field
C	Schwarz-Christoffel conformal modulus
c	concentration
D_L	longitudinal dispersion coefficient
D_{12}	binary diffusion coefficient
D^*_L	normalized longitudinal dispersion coefficient
D_{L0}	longitudinal dispersion with no convection
$D^*_{L,\text{fit},i}$	functional fit value of normalized longitudinal dispersion coefficient
$D^*_{L,\text{sim},i}$	simulation value of normalized longitudinal dispersion coefficient
$\boldsymbol{d}$	right-hand-side vector of difference system of equations
$\boldsymbol{d}_i$	right-hand-side vectors of tridiagonal system
$\boldsymbol{d}^i_x$	right-hand-side vector for i^{th} iteration of x-field

$\boldsymbol{d}_y^i$	right-hand-side vector for i^{th} iteration of y-field
dof	degrees of freedom
$\boldsymbol{E}$	electric field vector
$f(z)$	Schwarz-Christoffel mapping function
$f_{\text{top}}(x)$	functional definition of the top of the periodic domain
$f_{\text{bot}}(x)$	functional definition of the bottom of the periodic domain
$\hat{\imath}, \hat{\jmath}, \hat{k}$	directional unit vectors in physical space
$\boldsymbol{J}$	Jacobian matrix
J	Jacobian determinant
M	number of data points in χ^2 calculation
m	vertical scale of geometrical obstruction
N	number of particles used in Monte Carlo simulation
n	exponent on Péclet number
n_2	parameter in second fit function
n_e	parameter in second fit function for results from Edwards et al.
$\boldsymbol{n}$	vector normal to wetted perimeter of periodic domain
n_x, n_y	components of normal vector
$P(\bullet)$	probability function
Pe	Péclet number
Pe_c	critical Péclet number
$\text{Pe}_{c,01}$	critical Péclet number
$\text{Pe}_{c,02}$	critical Péclet number
$\text{Pe}_{c,12}$	critical Péclet number
Pe_e	Péclet number for results from Edwards et al.
p	wetted perimeter
Q_{BT}	flowrate from block-Thomas velocity solution
Q_{SC}	flowrate from Schwarz-Christoffel velocity solution
Q_ψ	flowrate from maximum value of the stream function
Q_u	flowrate from integration of the velocity field
q	charge
R	normally distributed random variable
R_1, R_2	normally distributed random variables from Box-Muller method
r	capillary radius
r_{xy}	length of spatial diffusion step
$r_{\phi\psi}$	length of inverse diffusion step
$\boldsymbol{S}$	finite difference matrix
$\boldsymbol{S}_x^i$	block-tridiagonal difference matrix for i^{th} iteration of x-field
$\boldsymbol{S}_y^i$	block-tridiagonal difference matrix for i^{th} iteration of y-field
t	time
Δt	hard-coded time-step
δt	high velocity integration time-step
U_1, U_2	uniform distributed random variables input into Box-Muller method
$\boldsymbol{u}$	velocity vector
$\boldsymbol{u}_{EP,i}$	electrophoretic velocity vector of i^{th} species
$\boldsymbol{u}_{EO}$	electroosmotic velocity vector
$\boldsymbol{u}_i$	velocity vector of i^{th} species
$\bar{u}$	mean solvent velocity
u_i	velocity of i^{th} species

u	x-component of velocity
$\boldsymbol{v}$	unknown vector in finite difference scheme
$\boldsymbol{v}_i$	unknown vectors of tridiagonal system
v	y-component of velocity
$W(z)$	complex function
$\boldsymbol{w}_i$	intermediate vector used in block-Thomas algorithm
x	longitudinal variable
$\delta\boldsymbol{x}$	spatial step in physical space
$\delta x, \delta y$	components of spatial step
$x(\phi, \psi)$	x-field
(x, y)	physical space coordinates
y	laterial variable
$y(\phi, \psi)$	y-field
$\boldsymbol{Z}_i$	intermediate matrix used in block-Thomas algorithm
z_k	Schwarz-Christoffel prevertices
z	complex variable

Chapter 1

Introduction

1.1 Motivation

Liquid chromatography is a multi-billion dollar industry and is a general-purpose technique for preparative and analytical chemistry. Recent advances in microtechnology clearly show that decreased size and integration of chromatography systems is possible. These are often termed "lab-on-a-chip" or "Micro Total Analysis" systems (μTAS) [1]. In particular, microfabrication technology allows for precisely defined chromatography column geometries on a single chip which were previously limited to capillaries joined together by various types of fittings. In numerous chromatography models, the capillary is packed with particles for increased mass transfer to surfaces. The advent of microchip columns allows these packings to be replaced by precision microfabricated posts (Figure 1-1(a)). These geometries allow separation of species on the basis of their interactions with these coated surfaces. In other separation modes, the channel is ideally perfectly straight, but surface imperfections are an unintended consequence of the microfabrication process (Figure 1-1(b)).

As a solute distribution travels through a microchannel, its mean position will be translated at the mean fluid velocity and the distribution will spread due to the combination of Brownian diffusion and gradients in the velocity field. These velocity gradients can be caused by pressure gradients, geometric irregularities, electric field irregulatiries, and irregularities in the electrochemistry of the fluid-solid interface. This combination of diffusive and convective effects on solute transport is known as hydrodynamic dispersion.

It is important to understand the longitudinal dispersion of solute in chromatography media because of its effects on species resolution. The resolution of a chromatography system is directly related to the ratio of the width of a single species distribution (band) and inversely related to

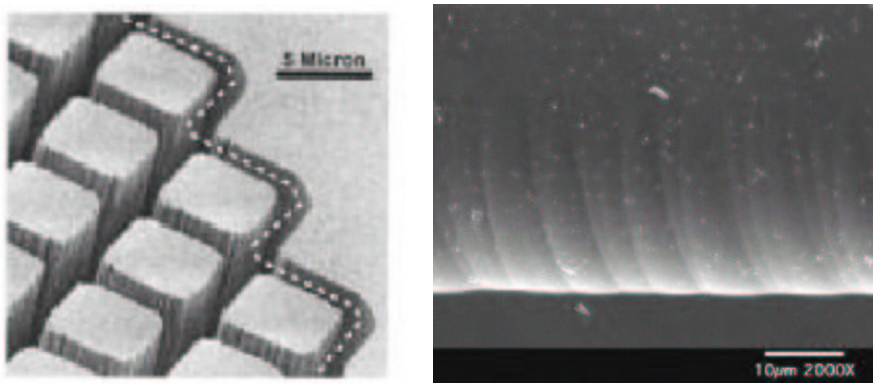

(a) Spatially-periodic geometry [2]. (b) Microfabrication imperfections.

Figure 1-1: Electron micrographs of microfluidic channels.

the distance between bands. The width of a band is the root-sum-square of contributions to band broadening from various sources [3]. When the initial band width and longitudinal dispersion are dominant

$$\delta_i = \sqrt{\delta_{0,i}^2 + 2D_{L,i}t}, \tag{1.1}$$

where $\delta_{0,i}$ is the initial band, $D_{L,i}$ is the longitudinal dispersion coefficient, and t is time. In microfluidic systems, $\delta_{0,i}$ can be controlled to less than 10 μm if desired. Thus, in most microchip chromatography applications, D_L is the dominant source of band broadening and therefore loss of resolution and expense of separation. The distance between distributions is

$$\Delta_{ij} = (u_i - u_j)t, \tag{1.2}$$

where u_i and u_j are the velocities of species i and j. For complete species resolution, $\Delta_{ij} \gg \delta_i$ and $\Delta_{ij} \gg \delta_j$. As an illustrative example, Figures 1-2 show three substances with different velocities and diffusivities separating in a chromatography column. At $t = 2$, Figure 1-2(b) shows the substance with the highest velocity moves away from the other two and is almost fully resolved by $t = 4$ (Figure 1-2(c)). The other two substances have similar velocities and relatively high diffusion, thus separation will take more time.

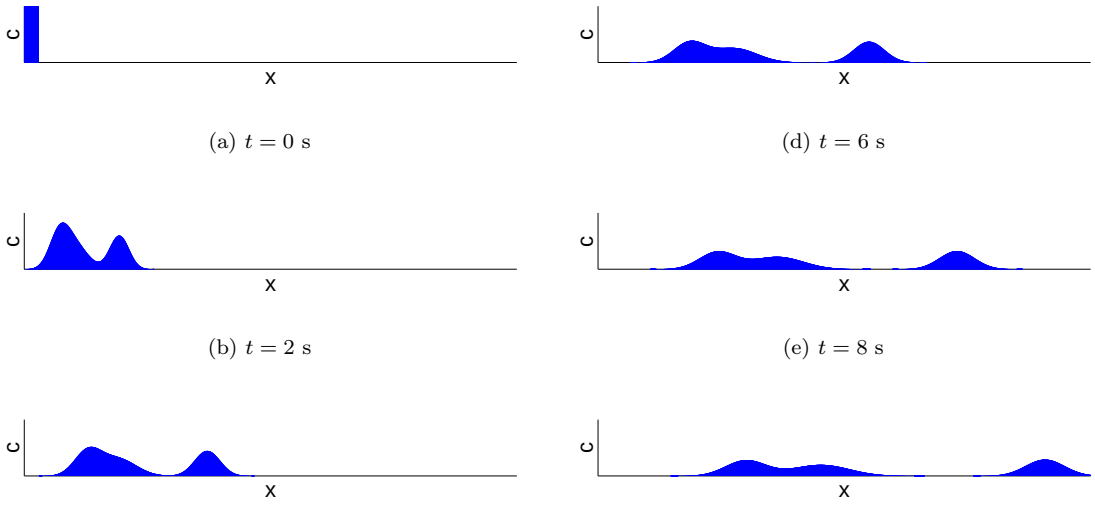

(a) $t = 0$ s (d) $t = 6$ s

(b) $t = 2$ s (e) $t = 8$ s

(c) $t = 4$ s (f) $t = 10$ s

Figure 1-2: Representation of a time series of chromatography separation of three species (concentration versus distance). The velocities and binary diffusivities of the three species are 1, 1.53, and 3.13 m/s and 10^{-1}, 2×10^{-1}, and 9×10^{-2} m^2/s from left to right. For a real chromatography system, the velocities are on the order of 1 mm/s and the diffusivities on the order of 10^{-9} m^2/s. The values used in this example were chosen to illustrate the concepts of band broadening and separation. Typical velocities for actual applications range from 10^{-5}–10^{-3} m/s and typical binary diffusivities from 10^{-9}–10^{-12} m^2/s. Depending on the channel height used (10^{-6}–10^{-5} m typical), the Péclet number can be as high as 10^3 for some proteins.

1.2 Microfluidics, chromatography, & dispersion

Manz [1] gives scaling laws relevant to miniaturization of total chemical analysis systems. Tables of scalings for both time-constant and time-scaled systems are presented. Time-constant means that the time scale is independent of length scale, whereas time-scaled means that time is reduced with a reduction in size. It is clear that by performing sample transport on micron scales rather than centimeter or millimeter scales, the time needed to move samples decreases and diffusion can be minimized, which maximizes resolution. An additional benefit of scaling down chemical analysis systems is that electroosmotic flow can be used to transport samples with less dispersion than pressure-driven flow. Rice et al. [4] shows that electroosmotic flow can be approximated by potential flow outside of a thin boundary layer called the Debye layer. Cummings et al. [5] and Santiago [6] provide additional analytical and experimental support for similitude between velocity and electric field outside of the Debye layer.

Because electroosmotic flow in a straight capillary has no gradient outside of a thin boundary layer, the longitudinal hydrodynamic dispersion coefficient will be approximately equal to the binary diffusion coefficient $D_L \simeq D_{12}$. However, turns, junctions, periodic structure, or other geometric irregularities will cause velocity gradients and thus contribute to higher dispersion. Turns can be used to make a microfluidic analysis system more compact. Culbertson et al. [7] gives a model for this turn-induced dispersion. Griffiths et al. [8, 9] uses a Monte Carlo particle tracking method as well as an inverse formulation whereby the velocity field is solved in (ϕ, ψ)-space and converted back to physical-space (x, y). Dutta et al. [10] also proposes geometries for low dispersion in pressure-driven microfluidics applications. In addition to turns, Griffiths et al. [9] discusses dispersion induced by junctions.

1.3 Taylor-Aris dispersion

Work on hydrodynamic dispersion by Taylor [11] considered a thin, cylindrical plug of solute in a capillary convected by laminar Poiseuille flow and neglected axial diffusion. Taylor found a relation between longitudinal dispersion D_L and Péclet number Pe:

$$\frac{D_L}{D_{12}} = \frac{\mathrm{Pe}^2}{48}, \tag{1.3}$$

where $\mathrm{Pe} = \frac{\bar{u}r}{D_{12}}$ is based on mean solvent velocity, capillary radius, and binary diffusion coefficient. In [12], two conditions on the validity of Equation 1.3 were found. The first gives the Péclet number

limit for which Equation 1.3 is valid

$$\mathrm{Pe} \gg \sqrt{48}. \tag{1.4}$$

The second gives the time needed for fully developed dispersion

$$t \gg \frac{r^2}{4D_{12}}. \tag{1.5}$$

Using an analysis of the moments of the solute distribution, Aris [13] eliminated the Péclet number restriction and gave the following result known as the Taylor-Aris dispersion relation

$$\frac{D_L}{D_{12}} = 1 + \frac{\mathrm{Pe}^2}{48}. \tag{1.6}$$

This approaches Equation 1.3 in the limit of large Péclet number. Additionally, for small Péclet number, Equation 1.6 tends toward pure diffusion. Aris [13] also showed that for any unidirectional flow, dispersion takes the following form

$$\frac{D_L}{D_{12}} = 1 + \frac{\mathrm{Pe}^2}{\alpha}, \tag{1.7}$$

where α is some constant. For two-dimensional Poiseuille flow between two plates, Wooding [14] finds

$$\frac{D_L}{D_{12}} = 1 + \frac{\mathrm{Pe}^2}{210}, \tag{1.8}$$

where the Péclet number is based on the height between the plates.

Since the work by Taylor [11, 12] and Aris [13], numerous papers have confirmed, refined, and extended work on hydrodynamic dispersion. Bournia et al. [15] found deviations from Aris' result (Equation 1.6) at low velocities. These deviations may be caused by neglecting axial diffusion. Bailey et al. [16] found similar deviations using both numerical and experimental methods.

Also, several papers have dealt with the early-time behavior of dispersion. Lighthill [17] developed a theory to characterize early-time behavior of solute in Poiseuille flow. Also on the topic of early-time dispersion, Latini et al. [18] discusses anomalous dispersion of a point-source in Poiseuille flow. The variance σ^2 of the solute distribution for very early times is shown to be diffusion dominated and not so affected by shear

$$\sigma^2 = 2D_{12}t, \tag{1.9}$$

whereas dispersion at late times agrees with Taylor and Aris

$$\sigma^2 = 2D_L t. \tag{1.10}$$

However, at intermediate times, the variance goes with a higher power of t

$$\sigma^2 = \frac{8\bar{u}^2}{3r^2} D_{12} t^3, \tag{1.11}$$

where $\bar{u}$ is the mean velocity and r is the capillary radius. In this regime, shear has become important, but the solute has yet to interact with the walls of the capillary.

1.4 Hydrodynamic dispersion in porous media

Because this work will address longitudinal dispersion in spatially-periodic geometries, literature on porous media provides a rich source of information. Fried et al. [19] gives extensive discussion on both longitudinal and lateral dispersion in porous media and Adler [20] discusses asymptotic analysis of dispersion in porous media. Brenner [21] develops a moment-based description of dispersion similar to that of Aris but for the more general flows found in spatially-periodic porous media. Brenner's method involves solving the following equation on a unit domain of the porous medium

$$\bar{u} + (\boldsymbol{u} \cdot \boldsymbol{\nabla}) B = D_{12} \Delta^{xy} B \tag{1.12}$$

subject to the following boundary conditions

$$(\boldsymbol{n} \cdot \boldsymbol{\nabla}) B = 0 \text{ on } p, \tag{1.13a}$$

$$B(x + \lambda, y) - B(x, y) = -\lambda, \tag{1.13b}$$

$$\boldsymbol{\nabla} B|_{x+\lambda,y} - \boldsymbol{\nabla} B|_{x,y} = 0, \tag{1.13c}$$

where $\bar{u}$ is the Darcy-scale mean velocity vector of the fluid, $\boldsymbol{u}$ is the local velocity vector field, $\boldsymbol{n}$ is a vector normal to the wetted perimeter p, $\boldsymbol{\nabla}$ and Δ^{xy} are the gradient and Laplacian operators, λ is the domain width, and B is a scalar field used to find the dispersion as follows

$$\frac{D_L}{D_{12}} = \frac{1}{A} \int_A |\boldsymbol{\nabla} B|^2 \, \mathrm{d}x\mathrm{d}y. \tag{1.14}$$

This method was used by Hoagland et al. [22] to analyze Taylor-Aris dispersion in a tube with sinusoidally varying boundaries as a simplified model of a porous medium.

Edwards et al. [23] summarizes the development in [21] and generates data for various geometries for comparison to both previous theory and experiment and discuss the possibility that $D_L \propto \mathrm{Pe}^n$, stating that $n \to 2$ as $\mathrm{Pe} \to \infty$. In addition, Eidsath et al. [24] presents data for dispersion in

packed beds, also noting $D_L \propto \mathrm{Pe}^n$ behavior with $n < 2$ for both experimental and numerical results. Probstein [25] gives a concise summary of the results from Taylor and Aris and discusses the practical limitations that Taylor-Aris dispersion sets on chromatography systems. In contrast to Equation 1.7, Probstein states that a more general flow will have $D_L \propto \mathrm{Pe}^n$ dependence where $1 < n < 2$. Kaviany [26] also discusses $D_L \propto \frac{\mathrm{Pe}^n}{\alpha}$ dependence, and states that α is some measure of the transverse gradient of the flow.

1.5 Outline and scope

Even in irrotational flows, distortions to the velocity field cannot always be avoided. Thus, longitudinal dispersion must be understood for better sample control in microfluidic systems. The goal of this thesis is to characterize different spatially periodic geometries in terms of longitudinal dispersion coefficients and Péclet number.

Two classes of geometries will be studied. The first represent in-line and staggered periodic post arrays with circular, square, and diamond shapes, similar to the geometry shown in Figure 1-1(a). The second class represents capillary tubes with a periodic sinusoidal or sawtooth boundary. The dichotomy used in separating the two classes has no bearing on the method of solution. Each has an easily defined periodic domain in which the velocity field may be solved. This velocity field will be used along with a Monte Carlo diffusion process to simulate dispersion at various values of Pe.

The goals of this thesis are the following:

- Develop method to calculate a velocity field in a periodic domain.
- Simulate particle transport through deterministic convection and random diffusion processes.
- Calculate longitudinal dispersion coefficients over range of Pe.
- Fit simulation results to polynomial functions that depend on Pe.
- Identify trends in fit parameters.
- Compare and contrast results with those in the literature.

Chapter 2

Mathematical formulation

2.1 Flow field solution

2.1.1 Spatially-periodic geometries

2.1.1.1 Post arrays

Figures 2-1 show the geometries of the periodic post arrays considered. In addition to post shape (diamond, circle, square) and array configuration (in-line, staggered), the post size is a third degree of freedom for these geometries. These geometries represent chromatography beds such as that shown in Figure 1-1(a). These geometries are useful for separations that involve interactions between the solute and the surfaces of the posts.

2.1.1.2 Capillary tubes

Figures 2-2 show the periodic capillary geometries. As with the post arrays, the amplitude of the boundary function is a degree of freedom. These geometries can be used to model imperfections in the fabrication process as in Figure 1-1(b) and also to understand how simple periodic disturbances affect dispersion in capillary flow.

2.1.2 Electrophoresis & electroosmosis in TDL limit

2.1.2.1 Electrophoresis

Following Probstein [25], the electrophoretic velocity $\boldsymbol{u}$ of a particle of charge q is found by equating the electrical force to the Stokes drag

$$q\boldsymbol{E} = 6\pi\rho\nu a\boldsymbol{u}, \tag{2.1}$$

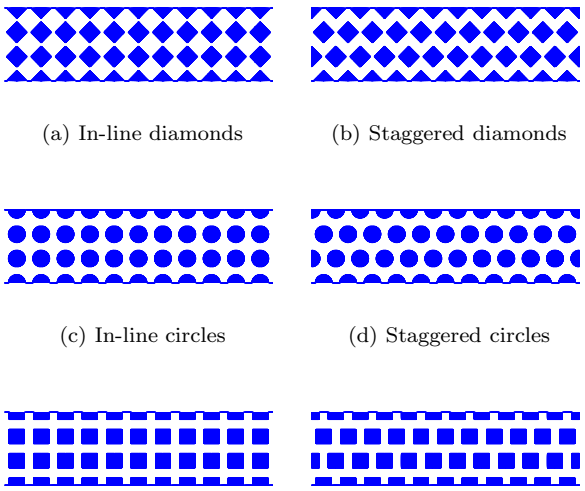

(a) In-line diamonds (b) Staggered diamonds

(c) In-line circles (d) Staggered circles

(e) In-line squares (f) Staggered squares

Figure 2-1: Spatially-periodic post arrays.

where $\boldsymbol{E}$ is the electric field, ρ is the fluid density, ν is the fluid viscosity, and a is the particle radius. This relationship can be rearranged to give the electrophoretic velocity of the i^{th} species

$$\boldsymbol{u}_{EP,i} = \mu_{EP,i}\boldsymbol{E}, \tag{2.2}$$

where $\mu_{EP,i} = \frac{q_i}{6\pi\rho\nu a_i}$ is the electrophoretic mobility of the i^{th} species. Equation 2.2 holds not only for particles, but is experimentally found to describe the motion of charged ions in solution.

2.1.2.2 Electroosmosis

Similarly, Cummings et al. [5] derived the result that the velocity field is everywhere similar to the electric field in the thin-Debye-layer (TDL) limit provided there is no pressure gradient in the system

$$\boldsymbol{u}_{EO} = \mu_{EO}\boldsymbol{E}, \tag{2.3}$$

where μ_{EO} is the electroosmotic mobility. This result was verified experimentally by Santiago [6].

Combining Equations 2.2 and 2.3, the total velocity of the i^{th} species is

$$\boldsymbol{u}_i = \mu_i\boldsymbol{E}, \tag{2.4}$$

where $\mu_i = \mu_{EP,i} + \mu_{EO}$ is the total mobility of the i^{th} species. The electric field can be rewritten

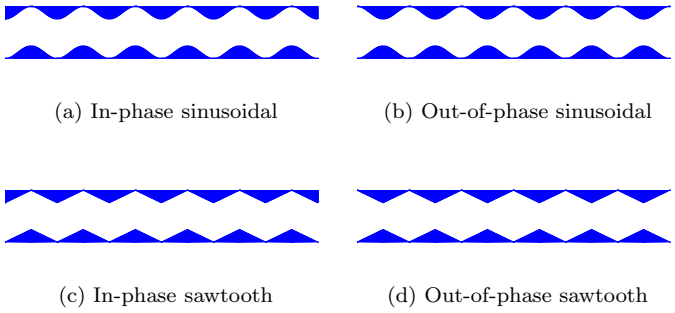

(a) In-phase sinusoidal (b) Out-of-phase sinusoidal

(c) In-phase sawtooth (d) Out-of-phase sawtooth

Figure 2-2: Spatially-periodic capillaries.

as the gradient of the electric potential Φ

$$\boldsymbol{u}_i = \mu_i \boldsymbol{\nabla} \Phi. \tag{2.5}$$

The velocity of a species can thus be expressed as the gradient of a scalar field and the curl of the velocity is identically zero outside of the Debye layer. This fact along with the incompressibility of the fluid allows the velocity field to be found from potential flow theory.

2.1.3 Analysis of potential flow

Assuming the thin Debye layer limit, the bulk flow can be treated as both irrotational and incompressible [4, 5, 6]. The condition of irrotationality of a velocity field $\boldsymbol{u} = \hat{\boldsymbol{\imath}} u + \hat{\boldsymbol{\jmath}} v$ can be stated as

$$\boldsymbol{\nabla} \times \boldsymbol{u} = \boldsymbol{0}, \tag{2.6}$$

where $\boldsymbol{\nabla} = \hat{\boldsymbol{\imath}} \frac{\partial}{\partial x} + \hat{\boldsymbol{\jmath}} \frac{\partial}{\partial y}$. This implies that the velocity field can be written as the gradient of a scalar field called the velocity potential

$$\boldsymbol{u} = \boldsymbol{\nabla} \phi. \tag{2.7}$$

The condition of incompressibility of a velocity field can be stated as

$$\boldsymbol{\nabla} \cdot \boldsymbol{u} = 0. \tag{2.8}$$

The velocity field can thus be written as the curl of some vector field

$$\boldsymbol{u} = \boldsymbol{\nabla} \times \boldsymbol{\psi}. \tag{2.9}$$

In two dimensions, this vector field has only the z-component $\boldsymbol{\psi} = \hat{\boldsymbol{k}}\psi$. The scalar field ψ is called the stream function. Thus, the velocity field can be written in the following two forms:

$$\boldsymbol{u} = \hat{\boldsymbol{\imath}}\frac{\partial\phi}{\partial x} + \hat{\boldsymbol{\jmath}}\frac{\partial\phi}{\partial y}, \tag{2.10a}$$

$$\boldsymbol{u} = \hat{\boldsymbol{\imath}}\frac{\partial\psi}{\partial y} - \hat{\boldsymbol{\jmath}}\frac{\partial\psi}{\partial x}. \tag{2.10b}$$

From these two expressions, it is clear that the following equalities hold:

$$\frac{\partial\phi}{\partial x} = \frac{\partial\psi}{\partial y}, \tag{2.11a}$$

$$\frac{\partial\phi}{\partial y} = -\frac{\partial\psi}{\partial x}. \tag{2.11b}$$

These equations, known as the Cauchy-Riemann conditions, relate the real and imaginary parts of the complex function $W(z) = \phi(z) + i\psi(z)$ contained in the domain Ω on the complex plane $z = x + iy$ [27].

The governing equations that need to be solved for the flow field can be found by inserting the definition of the velocity potential (Equation 2.7) into the definition of incompressiblity (Equation 2.8)

$$\boldsymbol{\nabla}\cdot\boldsymbol{\nabla}\phi = \Delta^{xy}\phi = 0, \tag{2.12}$$

where $\boldsymbol{\nabla}\cdot\boldsymbol{\nabla} = \Delta^{xy}$ is the Laplacian operator in (x, y)-space

$$\Delta^{xy} = \frac{\partial^2}{\partial x^2} + \frac{\partial^2}{\partial y^2}. \tag{2.13}$$

The second governing equation can be found by taking the cross product of the definition of the stream function

$$\boldsymbol{\nabla}\times\boldsymbol{\nabla}\times\hat{\boldsymbol{k}}\psi = \boldsymbol{\omega}. \tag{2.14}$$

Using the irrotationality of the fluid $\boldsymbol{\omega} = \mathbf{0}$ and a vector identity[1], Equation 2.14 becomes

$$\Delta^{xy}\psi = 0. \tag{2.15}$$

The boundary conditions for Equations 2.12 and 2.15 on $\delta\Omega$ will need to be defined on a single domain of the spatially-periodic geometry. Symmetry on the inlet and outlet will make $\phi_{\text{in}} \equiv \phi(0, y)$

[1] $\boldsymbol{\nabla}\times\boldsymbol{\nabla}\times\boldsymbol{A} = \boldsymbol{\nabla}(\boldsymbol{\nabla}\cdot\boldsymbol{A}) - \Delta^{xy}\boldsymbol{A}$, but if $\boldsymbol{\nabla}\cdot\boldsymbol{A} = 0$, the identity can be simplified to $\boldsymbol{\nabla}\times\boldsymbol{\nabla}\times\boldsymbol{A} = -\Delta^{xy}\boldsymbol{A}$.

and $\phi_{\text{out}} \equiv \phi(1, y)$ constant values. The velocity potential will be normalized such that

$$\phi_{\text{in}} = 0, \tag{2.16a}$$

$$\phi_{\text{out}} = 1. \tag{2.16b}$$

Additionally, the stream function will have zero slope across the inlet and outlet,

$$\left(\frac{\partial \psi}{\partial x}\right)_{\text{in}} = 0, \tag{2.17a}$$

$$\left(\frac{\partial \psi}{\partial x}\right)_{\text{out}} = 0. \tag{2.17b}$$

Because flow cannot pass through the boundaries on the top and bottom, the gradient of ϕ must be perpendicular to these boundaries. This is expressed as

$$(\boldsymbol{\nabla}\phi \cdot \hat{\boldsymbol{n}})_{\text{top}} = 0, \tag{2.18a}$$

$$(\boldsymbol{\nabla}\phi \cdot \hat{\boldsymbol{n}})_{\text{bot}} = 0. \tag{2.18b}$$

Finally, Equations 2.11 imply that $\boldsymbol{\nabla}\phi$ and $\boldsymbol{\nabla}\psi$ are perpendicular. Thus, ψ_{top} and ψ_{bot} must be constant. ψ_{bot} can be defined as zero, but ψ_{top} cannot be specified *a priori* without overconstraining the problem

$$\psi_{\text{top}} = Q, \tag{2.19a}$$

$$\psi_{\text{bot}} = 0. \tag{2.19b}$$

where the flowrate Q couples the ϕ- and ψ-fields and will be found as a result of the solutions of Equations 2.12 and 2.15. Equations 2.12 and 2.15 and boundary conditions are shown graphically in Figure 2-3.

2.1.4 Inverse formulation

2.1.4.1 Solution of flow field in inverse space

The most straightforward way to solve Equations 2.12 and 2.15 numerically is to write the Laplacian terms as second-order central differences and solve using an iterative method with asymmetric stencils on the non-straight boundary. A more elegant solution can be found by posing the problem

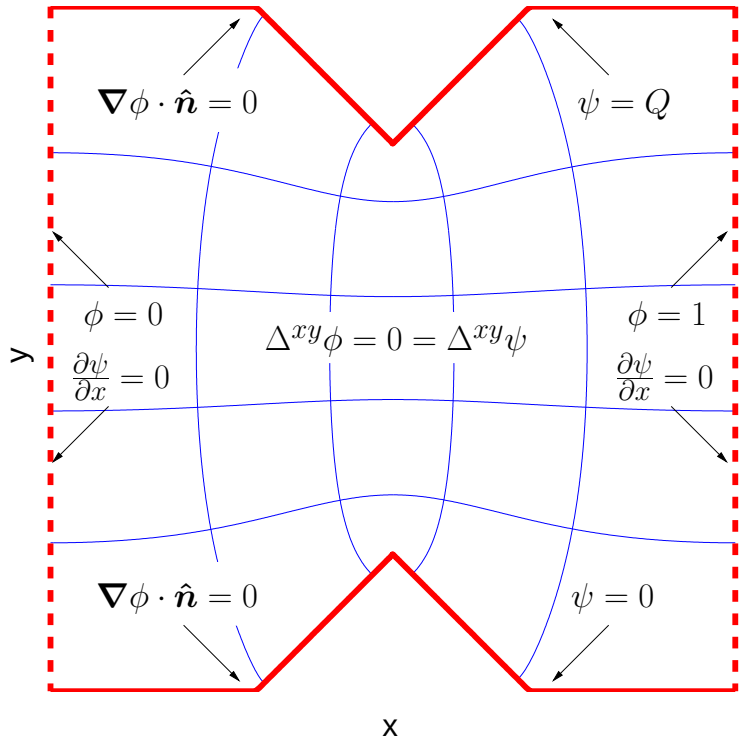

Figure 2-3: Diagram of governing equations and boundary conditions for an example geometry in (x, y)-space.

(ϕ, ψ)-space [8, 9, 28, 29]. Thus, the governing equations can be rewritten

$$\Delta^{\phi\psi} x(\phi, \psi) = 0, \tag{2.20a}$$

$$\Delta^{\phi\psi} y(\phi, \psi) = 0, \tag{2.20b}$$

where $\Delta^{\phi\psi}$ is the Laplacian operator in (ϕ, ψ)-space

$$\Delta^{\phi\psi} = \frac{\partial^2}{\partial\phi^2} + \frac{\partial^2}{\partial\psi^2}. \tag{2.21}$$

The benefit of this transformation is that the inverse of the boundary conditions given in Section 2.1.3 define a rectangular domain Ω' with aspect ratio Q. This rectangular boundary $\delta\Omega'$ eliminates the need for unevenly weighted differences in the numerical method used to solve for the flow field. To use the solutions to the above governing equations a relation between (ϕ, ψ)- and

(x, y)-space is needed. The following derivatives provide this relation [28]

$$\frac{\partial \phi}{\partial x} = \frac{1}{J}\frac{\partial y}{\partial \psi}, \tag{2.22a}$$

$$\frac{\partial \phi}{\partial y} = -\frac{1}{J}\frac{\partial x}{\partial \psi}, \tag{2.22b}$$

$$\frac{\partial \psi}{\partial x} = -\frac{1}{J}\frac{\partial y}{\partial \phi}, \tag{2.22c}$$

$$\frac{\partial \psi}{\partial y} = \frac{1}{J}\frac{\partial x}{\partial \phi}, \tag{2.22d}$$

where J is the determinant of the Jacobian matrix $\boldsymbol{J}$ (J is also simply referred to as the Jacobian)

$$J = \left|\frac{\partial(x, y)}{\partial(\phi, \psi)}\right| = \begin{vmatrix} \frac{\partial x}{\partial \phi} & \frac{\partial x}{\partial \psi} \\ \frac{\partial y}{\partial \phi} & \frac{\partial y}{\partial \psi} \end{vmatrix}. \tag{2.23}$$

To make this problem well-posed in (ϕ, ψ)-space, the boundary conditions for Equations 2.12 and 2.15 need to be inverted. The inlet and outlet condition for the y-field can be found by inverting the conditions in Equation 2.17 using Equations 2.22

$$\left(\frac{\partial y}{\partial \phi}\right)_{\text{in}} = 0, \tag{2.24a}$$

$$\left(\frac{\partial y}{\partial \phi}\right)_{\text{out}} = 0. \tag{2.24b}$$

The inlet and outlet boundary conditions for the x-field are constants

$$x_{\text{in}} = 0, \tag{2.25a}$$

$$x_{\text{out}} = 1. \tag{2.25b}$$

The boundary conditions for the top and bottom of the y-field are defined by the shape of the Ω for the particular geometry under consideration

$$y_{\text{top}} = f_{\text{top}}(x), \tag{2.26a}$$

$$y_{\text{bot}} = f_{\text{bot}}(x). \tag{2.26b}$$

where $f_{\text{top}}(x)$ and $f_{\text{bot}}(x)$ are functional definitions of the top and bottom of $\delta\Omega$. Finally, the conditions on the x-field on the top and bottom boundaries are

$$\frac{\partial \phi}{\partial x} n_x + \frac{\partial \phi}{\partial y} n_y = 0, \tag{2.27}$$

where n_x and n_y are the components of the surface normal vector $\hat{\boldsymbol{n}}$. Using Equations 2.22 this condition can be written

$$\frac{\frac{\partial x}{\partial \psi}}{\frac{\partial y}{\partial \psi}} = \frac{n_x}{n_y}. \tag{2.28}$$

The ratio on the right-hand-side is simply the negative of the slope of the function defining the top or bottom boundary. Thus

$$\left(\frac{\frac{\partial x}{\partial \psi}}{\frac{\partial y}{\partial \psi}}\right)_{\text{bot}} = -f'_{\text{bot}}(x), \tag{2.29a}$$

$$\left(\frac{\frac{\partial x}{\partial \psi}}{\frac{\partial y}{\partial \psi}}\right)_{\text{top}} = -f'_{\text{top}}(x). \tag{2.29b}$$

The x- and y-fields are coupled through Equations 2.29. Equations 2.20 and boundary conditions are shown graphically in Figure 2-4.

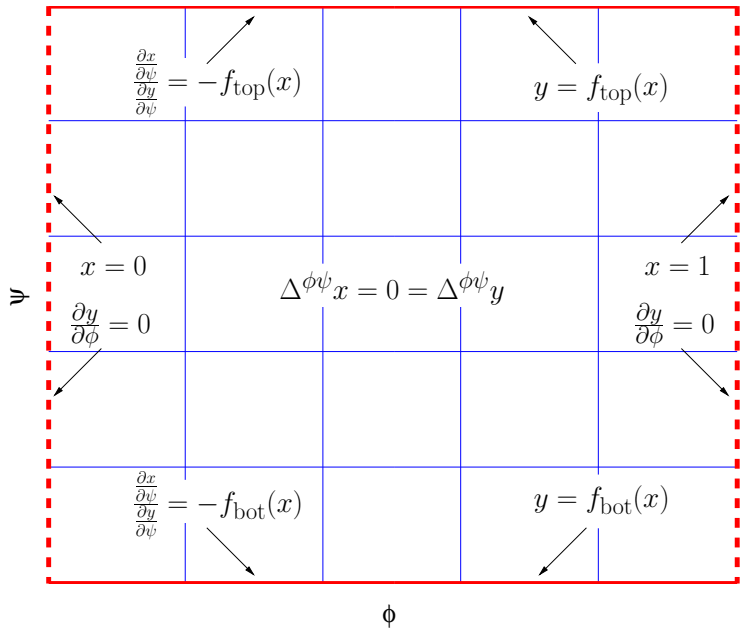

Figure 2-4: Diagram of governing equations and boundary conditions for an example geometry in (ϕ, ψ)-space.

2.2 Particle tracking in inverse space

2.2.1 Convection step

To avoid numerical error in calculating the velocities on the non-orthogonal (x, y)-mesh, the particle-tracking algorithm was developed for use in (ϕ, ψ)-space. Because the convection-step is a step along constant-ψ, the particles simply take a step $\delta\phi$, thus significantly reducing numerical dispersion transverse to streamlines. This convection-step can be approximated by a total differential

$$\delta\phi = \frac{\partial\phi}{\partial x}\delta x + \frac{\partial\phi}{\partial y}\delta y, \tag{2.30}$$

which can be rewritten

$$\delta\phi = \boldsymbol{\nabla}\phi \cdot \delta\boldsymbol{x}. \tag{2.31}$$

According to the definition of the velocity potential and recognizing that $\delta\boldsymbol{x} = \boldsymbol{u}\delta t$, this can be rewritten

$$\delta\phi = |\boldsymbol{u}|^2 \, \delta t. \tag{2.32}$$

Finally, noting that the Jacobian simplifies to $J = \frac{1}{|\boldsymbol{u}|^2}$, the convection step can be rewritten

$$\delta\phi = \mathrm{Pe} \cdot \frac{\delta t}{J}. \tag{2.33}$$

where the Péclet number acts as a non-dimensional velocity

$$\mathrm{Pe} = \frac{\overline{\Delta\phi}}{\Delta x}\frac{h}{D_{12}}. \tag{2.34}$$

2.2.2 Diffusion step

Next, the diffusion step in (ϕ, ψ)-space is needed. The length of the diffusion step r_{xy} is calculated from a normal distribution with zero mean

$$P(r_{xy}) = \frac{1}{\sigma\sqrt{2\pi}} \exp\frac{-r_{xy}^2}{2\sigma^2}, \tag{2.35}$$

where $\sigma = \sqrt{4\delta t}$[2]. The direction of the diffusion step θ_{xy} is taken from a uniform distribution

$$P(\theta_{xy}) = \left[-\frac{\pi}{2}, \frac{\pi}{2}\right]. \tag{2.36}$$

[2]The binary diffusion coefficient D is included in the Pe-scaling in the convection step. The extra factor of $\sqrt{2}$ in σ is from the two-dimensional nature of the problem [30].

The diffusion length can be written in terms of δx and δy as $r_{xy}^2 = \delta x^2 + \delta y^2$. The scaling of this step from (x, y)-space to (ϕ, ψ)-space can be found by replacing δx and δy by total derivatives and solving for $r_{\phi\psi}^2 = \delta\phi^2 + \delta\psi^2$. The result is

$$r_{\phi\psi} = \frac{r_{xy}}{\sqrt{J}}. \tag{2.37}$$

The angle will also be distorted in (ϕ, ψ)-space to $\theta_{\phi\psi}$. This angle is defined as

$$\theta_{\phi\psi} = \tan^{-1} \frac{\delta\psi}{\delta\phi}. \tag{2.38}$$

Writing $\delta\psi$ and $\delta\phi$ in terms of total differentials, $\theta_{\phi\psi}$ can be defined in terms of the local velocity field

$$\theta_{\phi\psi} = \tan^{-1} \left(\frac{u\delta y - v\delta x}{u\delta x + v\delta y} \right). \tag{2.39}$$

Chapter 3

Numerical methods

Dispersion driven by electroosmotic flow in spatially-periodic geometries was studied by performing Monte Carlo simulations of concentration-carrying particles being transported by convection and diffusion. Section 3.1 describes the solutions to the governing equations in Section 2.1 using two methods. The first is an inverse method [8, 9, 28] wherein the problem is formulated in (ϕ, ψ)-space, avoiding the problem of non-straight numerical boundaries. The second is the Schwarz-Christoffel transformation [27, 31, 32]. Section 3.2 describes the Monte Carlo method used to transport the particles in (ϕ, ψ)-space. Finally, Section 3.3 gives some results verifying the numerical methods.

3.1 Potential flow solution

3.1.1 Finite differences

Given $f_{\text{bot}}(x)$ and $f_{\text{top}}(x)$, Equations 2.20 can be solved using a second-order central difference scheme with a five-point stencil [33]. Assuming regular mesh spacings $\delta\phi$ and $\delta\psi$

$$\left(\Delta^{\phi\psi} x\right)_{jl} = \frac{x_{j+1,l} - 2x_{jl} + x_{j-1,l}}{\delta\phi^2} + \frac{x_{j,l+1} - 2x_{jl} + x_{j,l-1}}{\delta\psi^2} + O[\delta\phi^2] + O[\delta\psi^2]. \tag{3.1}$$

A simple first-order upwind or downwind difference scheme is used to approximate Neumann boundary conditions [33] in the difference matrix $\boldsymbol{S}$ (see Section 3.1.2).

$$\text{UW} : \left(\frac{\partial y}{\partial \psi}\right)_{jl} = \frac{y_{j,l+1} - y_{j,l}}{\delta\psi} + O[\delta\psi], \tag{3.2a}$$

$$\text{DW} : \left(\frac{\partial y}{\partial \psi}\right)_{jl} = \frac{y_{j,l} - y_{j,l-1}}{\delta\psi} + O[\delta\psi]. \tag{3.2b}$$

Where possible, first derivatives, such as those found in Equations 2.22, are solved using a second-order central difference scheme [33]. For example,

$$\left(\frac{\partial y}{\partial \psi}\right)_{jl} = \frac{y_{j,l+1} - y_{j,l-1}}{2\delta\psi} + O[\delta\psi^2]. \tag{3.3}$$

On boundary points, where a symmetric stencil is not possible, a second-order asymmetric difference scheme is used [29]

$$\left(\frac{\partial y}{\partial \psi}\right)_{jl} = \frac{-3y_{j,l} + 4y_{j,l+1} - y_{j,l+2}}{2\delta\psi} + O[\delta\psi^2]. \tag{3.4}$$

3.1.2 Block-Thomas algorithm

The solution to the Equation 3.1 can be solved as a linear system of equations

$$\boldsymbol{S}\boldsymbol{v} = \boldsymbol{d}, \tag{3.5}$$

where $\boldsymbol{v}$ is a vector of dimension $J \times L$ ($J = \frac{1}{\delta\phi} + 1$ and $L = \frac{Q}{\delta\psi} + 1$) containing the elements of the x- or y-field, $\boldsymbol{d}$ is a vector containing information about the boundary conditions, and $\boldsymbol{S}$ is a matrix of difference weights. The following is an example of $\boldsymbol{S}$ for a 3×3 grid and no boundary condition information

$$\boldsymbol{S} = \left(\begin{array}{ccc|ccc|ccc} -b & a & 0 & c & 0 & 0 & 0 & 0 & 0 \\ a & -b & a & 0 & c & 0 & 0 & 0 & 0 \\ 0 & a & -b & 0 & 0 & c & 0 & 0 & 0 \\ \hline c & 0 & 0 & -b & a & 0 & c & 0 & 0 \\ 0 & c & 0 & a & -b & a & 0 & c & 0 \\ 0 & 0 & c & 0 & a & -b & 0 & 0 & c \\ \hline 0 & 0 & 0 & c & 0 & 0 & -b & a & 0 \\ 0 & 0 & 0 & 0 & c & 0 & a & -b & a \\ 0 & 0 & 0 & 0 & 0 & c & 0 & a & -b \end{array}\right), \tag{3.6}$$

where $a = \frac{1}{\delta\psi^2}$, $b = 2\left(\frac{1}{\delta\phi^2} + \frac{1}{\delta\psi^2}\right)$, and $c = \frac{1}{\delta\phi^2}$. The horizontal and vertical lines show that $\boldsymbol{S}$ can be subdivided as a block-tridiagonal matrix. In general,

$$\boldsymbol{S} = \begin{pmatrix} \boldsymbol{B}_1 & \boldsymbol{C}_1 & & & & \\ \boldsymbol{A}_2 & \boldsymbol{B}_2 & \boldsymbol{C}_2 & & & \\ & \boldsymbol{A}_3 & \boldsymbol{B}_3 & \ddots & & \\ & & \ddots & \ddots & \ddots & \\ & & & \ddots & \ddots & \boldsymbol{C}_{L-1} \\ & & & & \boldsymbol{A}_L & \boldsymbol{B}_L \end{pmatrix}. \tag{3.7}$$

With $\boldsymbol{S}$ in this form, Equation 3.5 can be rewritten

$$\begin{pmatrix} \boldsymbol{B}_1 & \boldsymbol{C}_1 & & & & \\ \boldsymbol{A}_2 & \boldsymbol{B}_2 & \boldsymbol{C}_2 & & & \\ & \boldsymbol{A}_3 & \boldsymbol{B}_3 & \ddots & & \\ & & \ddots & \ddots & \ddots & \\ & & & \ddots & \ddots & \boldsymbol{C}_{L-1} \\ & & & & \boldsymbol{A}_L & \boldsymbol{B}_L \end{pmatrix} \begin{pmatrix} \boldsymbol{v}_1 \\ \boldsymbol{v}_2 \\ \boldsymbol{v}_3 \\ \vdots \\ \vdots \\ \boldsymbol{v}_L \end{pmatrix} = \begin{pmatrix} \boldsymbol{d}_1 \\ \boldsymbol{d}_2 \\ \boldsymbol{d}_3 \\ \vdots \\ \vdots \\ \boldsymbol{d}_L \end{pmatrix}. \tag{3.8}$$

This system can be solved using the block-Thomas algorithm [34] as follows

$$\begin{aligned} &\boldsymbol{Z}_1 = \boldsymbol{B}_1^{-1}\boldsymbol{C}_1, && \boldsymbol{Z}_k \left(\boldsymbol{B}_k - \boldsymbol{A}_k\boldsymbol{Z}_k\right)^{-1} \boldsymbol{C}_k, && k = 2, 3, \ldots, L-1 \\ &\boldsymbol{w}_1 = \boldsymbol{B}_1^{-1}\boldsymbol{d}_1, && \boldsymbol{w}_k \left(\boldsymbol{B}_k - \boldsymbol{A}_k\boldsymbol{Z}_k\right)^{-1} \left(\boldsymbol{d}_k - \boldsymbol{A}_k\boldsymbol{w}_{k-1}\right), && k = 2, 3, \ldots, L \\ &\boldsymbol{v}_L = \boldsymbol{w}_L, && \boldsymbol{v}_k = \boldsymbol{w}_k - \boldsymbol{Z}_k\boldsymbol{v}_{k+1}, && k = L-1, L-2, \ldots, 1. \end{aligned} \tag{3.9}$$

3.1.3 Iterative solution scheme

Because the equations for the x- and y-fields are coupled through Equation 2.29, an iterative solution is necessary. An initial guess for the x-field is made by assuming J equally-spaced vertical field lines. In addition, an initial flowrate of $Q = 1$ is used to determine $\delta\phi$. The values of x at the top and bottom of each field line are used to calculate the boundary values of y according to Equations 2.26. These values along with the boundary conditions from Equations 2.24 are used to construct a difference matrix $\boldsymbol{S}_y^1$ and a right-hand-side vector $\boldsymbol{d}_y^1$ for a set of equations $\boldsymbol{S}_y^1\boldsymbol{v}_y^1 = \boldsymbol{d}_y^1$. As explained in Section 3.1.2, this system can be solved using the block-Thomas algorithm.

The solution $\boldsymbol{y} = \boldsymbol{v}_y^1$ is used to adjust the flowrate through the channel as follows. A new $\delta\psi$ is found by considering the Cauchy-Riemann condition $\frac{\partial x}{\partial \phi} = \frac{\partial y}{\partial \psi}$. Taken along a line of constant-ψ,

such as the lower or upper boundary, the left-hand-side becomes a total derivative. This expression can now be integrated

$$\int_0^1 \mathrm{d}x = \int_{x=0}^{x=1} \left(\frac{\partial y}{\partial \psi}\right) \mathrm{d}\phi. \tag{3.10}$$

The integral of the left-hand-side taken across the periodic domain should be equal to one, but because Q has been overestimated, $\delta\psi$ is too large and the right-hand-side integral is less than one. The value of this integral is used to redefine the flowrate that defines a new $\delta\psi$ for the next iteration.

The new values for y can be used to define a difference matrix $\boldsymbol{S}_x^1$ and a right-hand-side vector $\boldsymbol{d}_x^1$ for a set of equations $\boldsymbol{S}_x^1 \boldsymbol{v}_x^1 = \boldsymbol{d}_x^1$. This difference matrix is also block-tridiagonal and can be solved using the block-Thomas algorithm. Using these new values for the x-field, a new difference matrix can be calculated for the y-field. This process is repeated until the residual of the numerical scheme in Equation 3.1 falls below a defined tolerance. Using Equations 2.22 to take derivatives of the x- and y-fields, the Jacobian and velocity fields can be found.

3.1.4 Schwarz-Christoffel transformation

The block-Thomas algorithm works well when $f_{\mathrm{top}}(x)$ and $f_{\mathrm{bot}}(x)$ are slowly varying, continuously differentiable functions or polygonal geometries with small interior angles. However, because of numerical instabilities, this method fails when $f_{\mathrm{top}}(x)$ and $f_{\mathrm{bot}}(x)$ do not meet these criteria. For these geometries, a different method is used to solve for the flow field.

The Schwarz-Christoffel transformation provides a means of mapping difficult geometries into simple geometries in the complex plane [27, 31, 32, 35]. The following equation provides the transformation from some n-sided polygon to a rectangle [36, 37, 38]

$$f'(z) = C\ \mathrm{sn}'(z) \prod_{k=1}^{n} \left[\mathrm{sn}(z) - \mathrm{sn}(z_k)\right]^{\alpha_k - 1}, \tag{3.11}$$

where $\mathrm{sn}(z)$ is the Jacobi elliptic function (also written $\mathrm{sn}(z|m)$), z_k are the *prevertices*[1], and α_k are the interior angles of the polygon. The conformal modulus C is the aspect ratio of the rectangle in the transformed space and is identical to the flowrate Q.

The above-stated problem can be solved using the Schwarz-Christoffel Toolbox for MATLAB [37, 38, 39]. This is a library of functions containing methods for solving a variety of Schwarz-Christoffel problems. For the purposes of this research, geometries were defined in the complex plane[2] and input to the rectangular mapping function which solves for $f(z)$. Values of the x- and

[1] A *prevertex* a vertex of the n-sided polygon in the transformed space.

[2] Squares and diamonds can be exactly defined with line segments. Each circle is a polygon made of 64 line segments.

y-fields for a regular grid of ϕ- and ψ-values can thus be found

$$x + iy = f(\phi + i\psi). \tag{3.12}$$

Difference schemes for first derivatives (Equations 3.3 and 3.4) can be used to find the Jacobian and velocity fields from the resulting x- and y-fields.

3.2 Particle tracking

3.2.1 Monte Carlo method

With the solution to the velocity fields in the spatially-periodic geometry, a Monte Carlo particle-tracking method was used to simulate the evolution of solute concentration with time [8, 9, 40]. Because a Monte Carlo method uses discrete particles to carry information about the solute concentration, the numerical diffusion and time-step instabilities associated with solving the full transport equation are avoided [8, 41, 42, 43]. In particular, as $\mathrm{Pe} \to \infty$ numerical diffusion from finite difference techniques can overwhelm the relatively small physical diffusion and the error of spectral methods becomes unbounded [43].

Figure 3-1 shows an example plot of the particles distributed in a geometry with in-line diamond post arrays. As mentioned in Section 2.2.2, the convection and diffusion steps are done in (ϕ, ψ)-space to reduce numerical diffusion transverse to the streamfunction. The simplest method would be to allow the particles to take a deterministic convection-step proportional to $\mathrm{Pe} \cdot \delta t$ and a random diffusion-step proportional to $R \cdot \sqrt{4\delta t}$ [8, 9, 40, 30, 44], where Pe is the Péclet number, R is a random number from a normal distribution, and δt is the time step. As in Section 2.2.2, the extra factor of $\sqrt{2}$ in the diffusion step is from the two-dimensional nature of the geometry [30]. To reduce statistical error, a split-step scheme was used [45]. Instead of a full convection-step followed by a full diffusion-step, a full convection-step is done between two half-diffusion-steps. The idea behind the split-step scheme is that diffusion is better modelled as a succession of smaller steps rather than one larger step.

Because the standard C library only has functions to generate uniform random numbers, the Box-Muller method was used to generate two normally distributed random numbers from two uniformly distributed random numbers [46, 47, 48]. Two uniform random variables, U_1 and U_2 are used to generate two uncorrelated normal random variables R_1 and R_2 as follows

$$R_1 = \sqrt{-2 \ln U_1} \cos 2\pi U_2, \tag{3.13a}$$

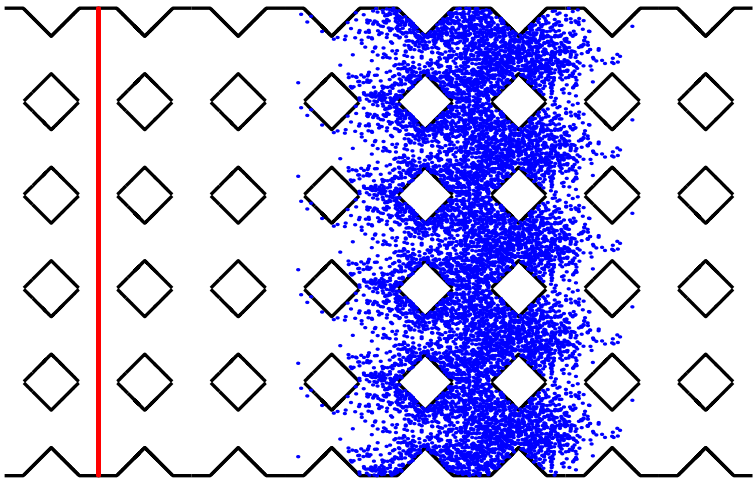

Figure 3-1: Distribution of $N = 2\ 000$ particles at $t = 0.05$ at $\mathrm{Pe} = 100$. The line on the left shows the initial positions of the particles. The computational domain and particle positions are copied five times in the vertical direction to convey a sense of the chromatography application.

$$R_2 = \sqrt{-2 \ln U_1} \sin 2\pi U_2. \tag{3.13b}$$

Conveniently, the two normal random variables generated by this method can be used in the two half-diffusion-steps.

In physical space, the condition of impermeability on the boundary would be enforced by checking that the y-position of each particle is within $f_{\mathrm{bot}}(x)$ and $f_{\mathrm{top}}(x)$. If a particle takes a random diffusion-step outside of the domain, it has to be reflected back. This can get complicated near corners and is simpler in inverse space where the top and bottom boundaries are simply horizontal lines. If the ψ-position of a particle is below 0, the sign of ψ is reversed. If the ψ-position of a particle is above Q, the ψ-position is reflected over $\psi = Q$.

3.3 Code validation

The program to solve for the x- and y-fields using the inverse formulation (Section 2.1.4) was written in C[3] using double precision and compiled using GNU gcc version 2.96 on an i386 computer with a Pentium 4 2.8GHz processor running Red Hat Linux 7.3. Solutions were found on a 301×301 rectangular grid in (ϕ, ψ)-space. This grid-size was chosen to minimize discretization error while staying within the bounds of available RAM (1GB) and time. The post array geometries geometries have large values of $f'_{\mathrm{top}}(x)$ and $f'_{\mathrm{bot}}(x)$ and thus flow fields for these domains could not be calculated

[3]Routines from Press et al. [49] and Lau [50] were used for memory allocation and matrix manipulation.

with the inverse formulation. These flow fields were solved using the Schwarz-Christoffel Toolbox for MATLAB (Section 3.1.4). Functions were written and the calculations were performed using MATLAB [51] running on an i386 computer with an AMD Athlon 1.2 GHz processor running Red Hat Linux 7.3. Solutions with this method were found on a 601×601 rectangular grid in (ϕ, ψ)-space. Finally, the particle tracking code (Section 3.2) was written in C and compiled as above. This code was run on the two above-mentioned computers.

3.3.1 Flow field verification

3.3.1.1 Solid boundary

MATLAB was used to perform various post-processing tests on the outputs of both potential flow solvers. The solid boundary conditions were checked by examining finite difference approximations of Equations 2.29. The slope of $f_{\text{bot}}(x)$ was compared to x- and y-differences in the ψ-direction

$$\frac{x_{jl} - x_{j,l-1}}{y_{jl} - y_{j,l-1}} = -\frac{y_{j+1,l} - y_{j-1,l}}{x_{j+1,l} - x_{j-1,l}}. \tag{3.14}$$

This can be rearranged as follows

$$\left(\frac{y_{jl} - y_{j,l-1}}{x_{jl} - x_{j,l-1}}\right) \cdot \left(\frac{y_{j+1,l} - y_{j-1,l}}{x_{j+1,l} - x_{j-1,l}}\right) = -1, \tag{3.15}$$

which is a statement that x- and y-field lines must be perpendicular[4]. This condition is guaranteed to be imposed by the block-Thomas algorithm and has a root-mean-squared (RMS) deviation of $O[10^{-5}]$. The Schwarz-Christoffel solution for the same geometry gives a slightly higher RMS value of $O[10^{-2}]$.

3.3.1.2 Orthogonality of x- and y-fields

Using Equations 2.22 it can be shown that lines of constant-x and constant-y are perpendicular

$$\boldsymbol{\nabla} x \cdot \boldsymbol{\nabla} y = 0, \tag{3.16}$$

where $\boldsymbol{\nabla}$ is the gradient in (ϕ, ψ)-space. This can be verified by applying Equation 3.16 to the discretized solutions of the x- and y-fields. This test assures that the x- and y-fields are correctly coupled. The block-Thomas algorithm gives an RMS difference of Equation 3.16 of $O[10^{-2}]$ compared with the Schwarz-Christoffel result of $O[10^{-3}]$, with most of the error in both cases occurring near

[4]This is true everywhere in the domain, not just on the boundary

regions where the hard boundary changes rapidly, such as corners.

3.3.1.3 Flowrate

One more simple verification that the block-Thomas algorithm and Schwarz-Christoffel method are consistent is to compare the flowrates of those geometries that can be calculated with either method. These geometries are the in-phase and out-of-phase sawtooth geometries in Figures 2-2(c) and 2-2(d). The flowrates are calculated by integrating the velocity at the inlet, middle, and outlet of the domain taking the average. A comparison of these flowrates (Table 3.1) shows that the two methods consistently predict the same flowrate within 1%. Tables of flowrates for all geometries are listed in Appendix A.

Table 3.1: Comparison of flowrates for sawtooth geometries calculated with both the block-Thomas algorithm Q_{BT} and Schwarz-Christoffel method Q_{SC}. m is the half-height of the sawtooth and A is the mean cross-section of the domain.

Geometry	m	A[a]	Q_{BT}	Q_{SC}	$\%_{\mathrm{diff}}$
In-phase	0.03	0.94	0.9360	0.9362	0.0214
	0.06	0.88	0.8643	0.8651	0.0925
	0.09	0.82	0.7856	0.7872	0.2033
	0.12	0.76	0.7008	0.7034	0.3696
Out-of-phase	0.03	0.94	0.9352	0.9367	0.1601
	0.06	0.88	0.8627	0.8658	0.3581
	0.09	0.82	0.7825	0.7877	0.6601
	0.12	0.76	0.6942	0.7028	1.2237

[a] $A = 1 - 2m$

3.3.2 Particle tracking verification

3.3.2.1 Number of particles

The split-step Monte Carlo convection-diffusion method described in Section 3.2 was tested for the case of Taylor-Aris dispersion in two-dimensions (Equation 1.8). This makes a good test case because the flow field can be solved for exactly and the dispersion relation is known exactly. Simulations were done using various values of N. The value of χ^2 (based on the method of maximum likelihood [48]) was used to quantify the goodness of fit between Equation 1.8 and the simulation results[5]. Based on this analysis, $N = 50\ 000$ was chosen (see Figure 3-2).

[5] A value of $\chi^2/\mathrm{dof} = 1$ indicates that the fit function is a good description of the data (see Section 4.1.3).

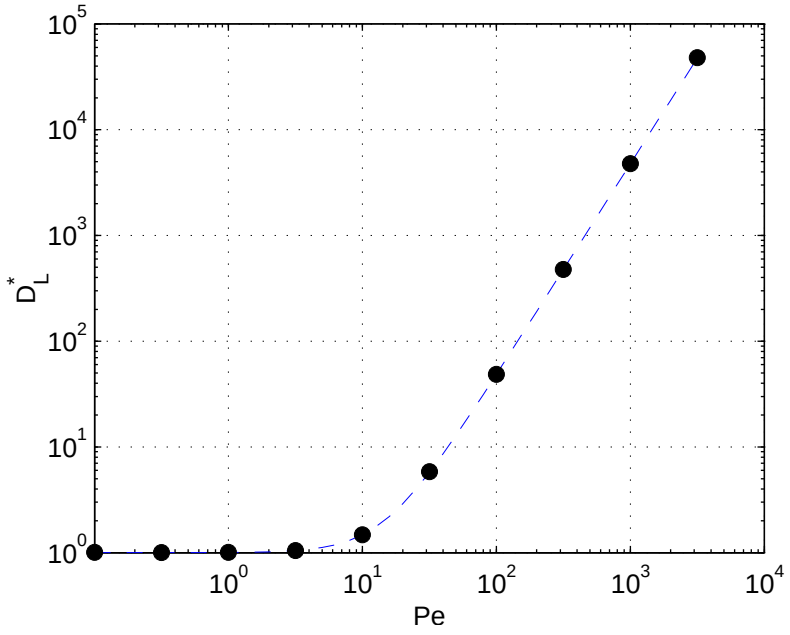

Figure 3-2: Comparison of simulation results and Equation 1.8 with $N = 50\ 000$ particles. The dashed line represents Equation 1.8; $\chi^2 = 0.19$.

3.3.2.2 Time-step independence

The size of the time-step Δt should be small enough such that further reduction will not significantly affect the result. Simulations of transport in the pure diffusion limit ($\mathrm{Pe} = 0$) were performed with various values of Δt until $t = 0.5$. The time-step selected $\Delta t = 10^{-4}$ was the largest for which independence was observed.

Using the time-step value above, $\delta\phi$ from Equation 2.33 may not be small compared to the domain size if the quantity $\frac{\mathrm{Pe}}{J}$ is large[6]. When the simple ϕ-step from Equation 2.33 is greater than 10^{-2}, an integration scheme is performed along a line of constant-ψ from the initial position ϕ_o to the final position $\phi_o + \delta\phi$:

$$\delta t = \frac{1}{\mathrm{Pe}} \int_{\phi_o}^{\phi_o + \delta\phi} J(\phi) \mathrm{d}\phi. \tag{3.17}$$

The kernel is discretely summed until the value of $\delta t = 10^{-4}$ and the final value of $\delta\phi$ becomes the value of the convection-step.

[6]Large values of $\frac{\mathrm{Pe}}{J}$ occur near convex corners where fluid acceleration is highest.

Chapter 4

Simulation procedure & results

4.1 Procedure

To explain the results, a complete description of the simulation procedure and data analysis is given for one case: an in-line circle post array with $m = 0.35$. Attention is then turned to comparing the results with those from other geometries.

4.1.1 Velocity field solution

The velocity field for the in-line circle post array is calculated by applying finite difference versions of Equations 2.11 to the potential flow solution from the Schwarz-Christoffel Toolbox for MATLAB [37]. A plot of ϕ and ψ in the physical domain is shown in Figure 4-1. The value of m associated with a given geometry is the size of the post (diamond height, circle radius, square height) or twice the magnitude of the sinusoid or sawtooth shape in the capillary. Plots of other domains can be found in Appendix B.

4.1.2 Calculation of longitudinal dispersion

Using the calculated velocity field for convection and the Box-Muller method to generate random variables for diffusion, 50 000 particles are transported in the periodic domain (Figures 4-2 and 4-3). At each time step of the simulation the (ϕ, ψ)-space positions of the particles are converted to (x, y)-space positions using a two-dimensional linear interpolation. These positions are used to calculate

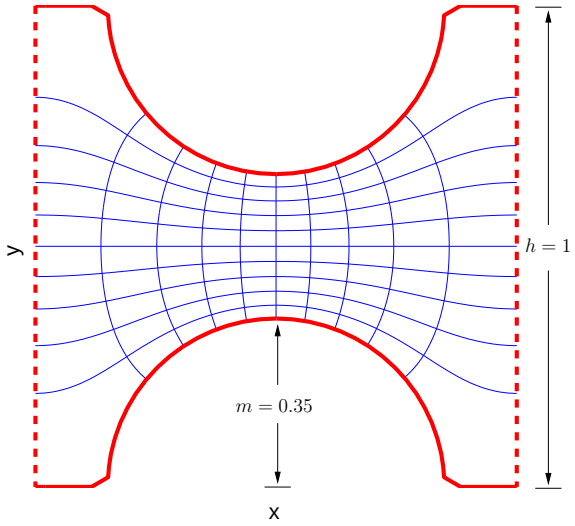

Figure 4-1: Contour plot of (ϕ, ψ) for in-line circles ($m = 0.35$). Note the cut corners at either end of the half-circles. This is an artifact of plotting the rectangular (ϕ, ψ)-mesh in (x, y)-space. Because grid points only exist at either side of the impingements of the half-circles and the $y = 0$ and $y = 1$ boundaries, the exact location of the impingement is not resolved. However, because the particle transport takes place in (ϕ, ψ)-space, where the top and bottom boundaries are horizontal lines, these cur corner contours have no effect on the simulation.

the variance σ^2 of the solute distribution

$$\sigma^2 = \frac{1}{N-1}\sum_{i}^{N}(x_i - \mu)^2 \tag{4.1}$$

and the error on the variance [52]

$$\sigma_{\sigma^2} = \sigma^2\sqrt{\frac{2}{N}}. \tag{4.2}$$

The slope[1] of time versus variance is calculated over the final 45% and 90% of the total time as shown in Figure 4-4. To ensure convergence over an order of magnitude, the simulation terminates when the percentage difference between these slopes falls below 0.5%. This slope is equal to twice the longitudinal dispersion coefficient $2D_L$ and the error on the slope is estimated to be $0.01 \cdot D_L$ (1%). For each individual geometry, simulations are performed at values of Pe from 10^{-1} to $10^{3.5}$ at half-decade intervals. Simulations are also performed at Pe = 0 to find D_{L0}, which is used to normalize ${D_L}^2$.

[1]This slope is calculated using a special case of maximum likelihood for straight lines [48].
[2]Values of D_{L0} are tabulated in Appendix C.

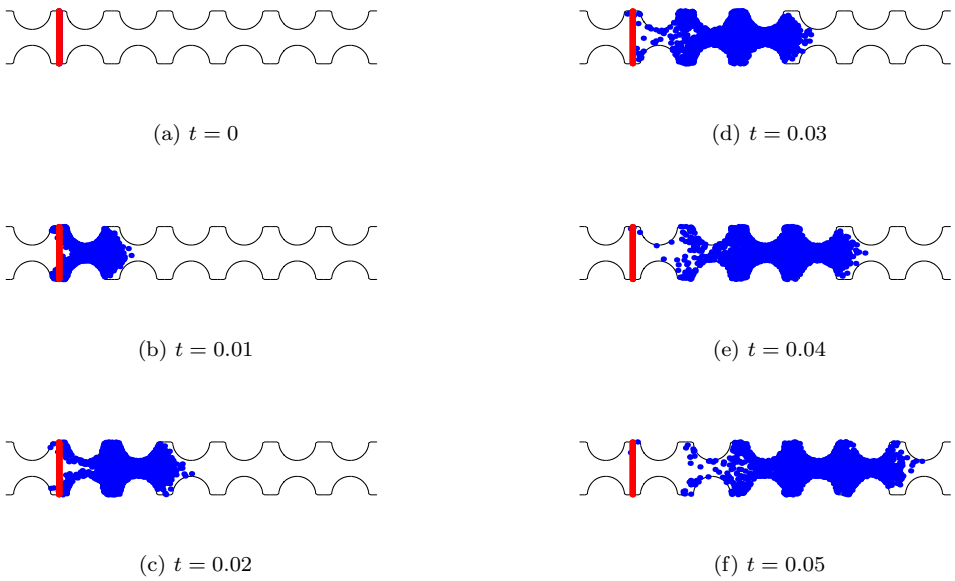

(a) $t = 0$ (d) $t = 0.03$

(b) $t = 0.01$ (e) $t = 0.04$

(c) $t = 0.02$ (f) $t = 0.05$

Figure 4-2: Time series of particle distributions in an in-line circle post array ($m = 0.35$, Pe $= 100$, $N = 2\ 000$). The lines on the left of each figure show the initial positions of the particles.

4.1.3 Functional fits to results

The values of $D_L^* = D_L/D_{L0}$ are plotted against Pe and fit by three equations with free parameters using the method of maximum likelihood [48]. The method of maximum likelihood seeks to find the values of the free parameters that minimize the value of χ^2

$$\chi^2 = \sum_{i=1}^{M} \left(\frac{D^*_{L,\text{fit},i} - D^*_{L,\text{sim},i}}{\sigma_{D^*_{L,i}}} \right)^2 , \tag{4.3}$$

where M is the number of data points used in the fit and $\sigma_{D^*_{L,i}}$ are the errors at each point. Strictly speaking, a function is said to describe the data well if the value of χ^2 divided by the degrees of freedom[3] (dof) equals unity. This was the criterion used for the numerical validation of the particle tracking method in Poiseuille flow in Section 3.3.2.

[3]The degrees of freedom is defined as the difference between the number of data points and the number of free parameters in the fit function.

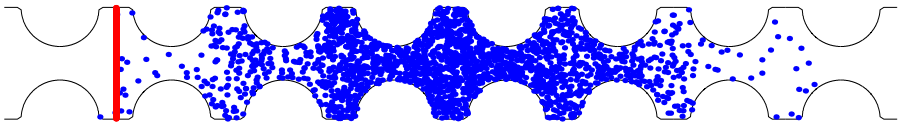

(a) Pe = 10

(b) Pe = 100

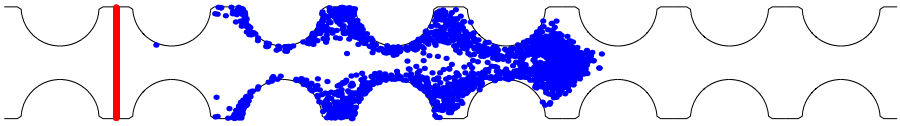

(c) Pe = 1000

Figure 4-3: Particle distributions at Pe = 10, 100, and 1000 with a longitudinal mean value of 3 (the width of one domain is 1). Note that as the Péclet number increases, the distribution stays more compact as with distance from the initial point.

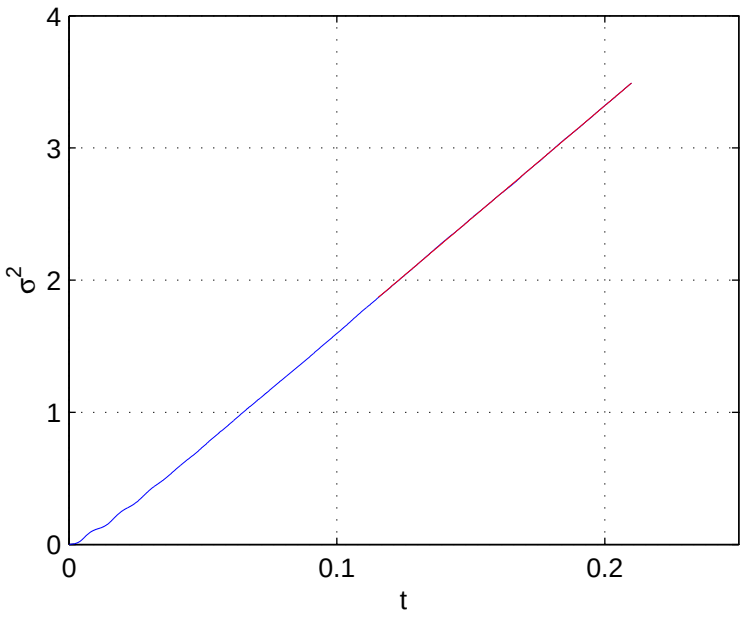

Figure 4-4: Longitudinal dispersion is found from the long-time limit of the slope of σ^2 versus t. In this case, Pe = 100, N = 50 000, and $D_L = 8.58$ for in-line circles with $m = 0.35$. The red curve indicates the final 45% of the domain over which D_L was calculated.

4.1.3.1 1st fit function: Taylor-Aris form

The form of the first fit function (see Figure 4-5) is suggested by Aris' result [13] for a unidirectional flow (Equation 1.7):

$$D_L^* = 1 + \frac{\mathrm{Pe}^2}{\alpha_1}. \tag{4.4}$$

This function should work best when the periodic geometry has only a small effect on the flow field. It is expected that as m increases, the dispersion will increase and the free parameter α_1 will decrease. However, it is also expected that as m increases, the flow will become less unidirectional, which breaks Aris' assumption for Equation 1.7. The failure of Equation 4.4 as a fit to the numerical results is manifested as an increase in α_1 at high m as seen in Table 4.1[4]. Although α_1 generally falls with increasing m, at large m the trend reverses itself for many geometries (see Figure 4-6) and the goodness of fit as measured by χ_1^2 becomes worse. The large value of χ_1^2 associated with large m indicates that for this set of results, Equation 4.4 does not describe the data well.

[4]The reasons for taking the roots of the parameters α_i will be explained below.

Table 4.1: Fit parameters and non-dimensional scales for in-line circles.

m	A^{a}	Λ	D_{L0}	$\sqrt{\alpha_1}$	χ_1^2	$\sqrt[n_2]{\alpha_2}$	n_2	χ_2^2	$\alpha_{3,1}$	$\sqrt{\alpha_{3,2}}$	$\frac{\alpha_{3,2}}{\alpha_{3,1}}$	χ_3^2
0.150	0.929	0.771	0.922	88	21	84	1.955	16	286	91	29	6
0.169	0.910	0.734	0.906	75	32	71	1.947	24	191	78	32	8
0.200	0.874	0.674	0.883	62	52	56	1.928	37	112	65	37	9
0.226	0.840	0.623	0.862	55	76	49	1.912	53	78	58	43	11
0.250	0.804	0.575	0.843	50	118	43	1.892	83	54	54	53	16
0.282	0.750	0.510	0.794	45	213	36	1.847	144	32	49	75	26
0.300	0.717	0.474	0.774	44	266	33	1.808	163	26	48	91	22
0.339	0.640	0.397	0.726	42	458	25	1.692	229	16	48	148	18
0.350	0.615	0.373	0.703	42	527	22	1.640	227	14	48	171	13
0.357	0.599	0.358	0.690	42	586	21	1.606	244	12	49	193	12
0.395	0.510	0.278	0.657	44	865	14	1.454	178	9	52	312	25

[a] $A = 1 - \pi m^2$

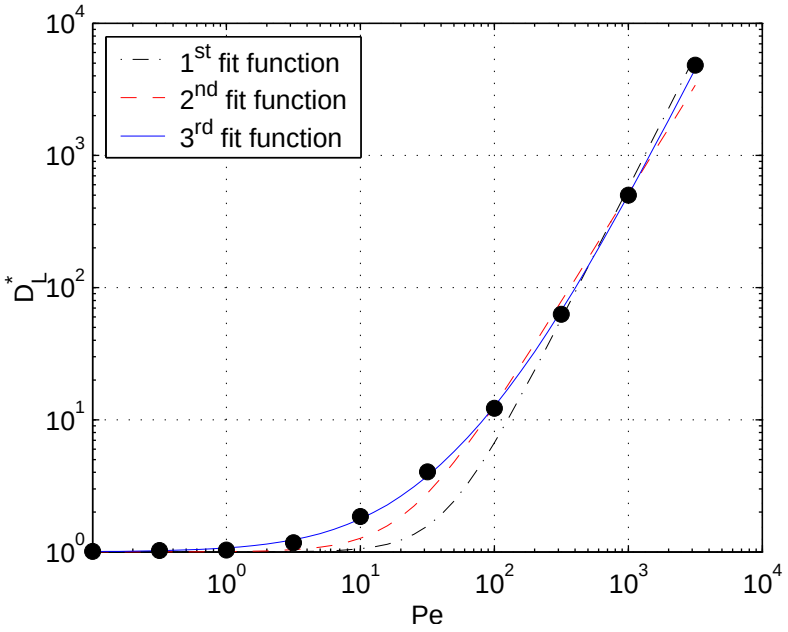

Figure 4-5: Best fit curves for in-line circle post array dispersion results at $m = 0.35$. For this and further figures, errors are estimated to be 1% and are smaller than the data marks on the plot. Equation 4.4 may be a good fit in the Pe $\to \infty$ limit, but works poorly for $10^0 <$ Pe $< 10^{2.5}$. Equation 4.5 fits the results better than Equation 4.4, but still has problems at $10^0 <$ Pe $< 10^2$ and misses the slope of the Pe $> 10^2$ points. Equation 4.6 has the necessary freedom to match the slowly varying slope in the middle Péclet range and still match the Pe^2 at high Péclet. Values for free parameters can be found in Table 4.1.

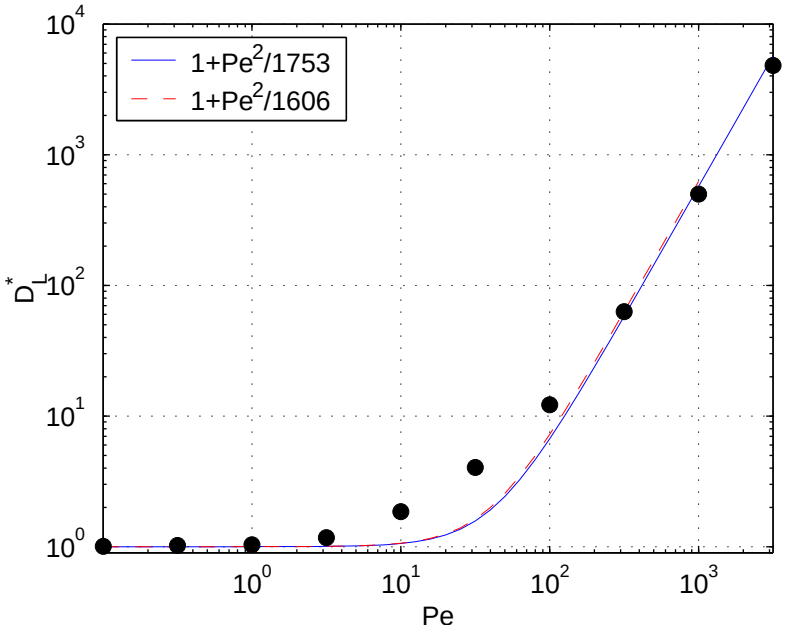

Figure 4-6: Simulation results and fits for in-line circles ($m = 0.35$). The dashed red curve does not include the last point ($\mathrm{Pe} = 10^{3.5}$). Increasing the range of Pe causes an increase in α_1 which shifts the curve to the right. This behavior is observed when the condition $\mathrm{Pe}_{\max} \gg \mathrm{Pe}_{c,12}$ is not met. Also note that in the range $10^{0.5} < \mathrm{Pe} < 10^2$, the dispersion has a slope of nearly one, but above that range, the slope is nearly two.

4.1.3.2 2nd fit function: porous media form

The second fit function (see Figure 4-5) has been suggested by the porous media community to deal with highly non-unidirectional flows [23, 24, 25, 26]:

$$D_L^* = 1 + \frac{\mathrm{Pe}^{n_2}}{\alpha_2}. \tag{4.5}$$

This function allows the non-unidirectional nature of the flow to be captured by the parameter n_2. Again, it is expected that α_2 will decrease with increasing dispersion and also that n_2 will start near a value of 2 and fall as the flow becomes less unidirectional. The results in Table 4.1 agree with these predictions. The value of χ_2^2 show that Equation 4.5 describes the results better than Equation 4.4. In most geometries the value of χ_2^2 peaks at a middle value of m and decreases afterward which may indicate that each geometry has a critical value of m for which the character of the flow changes.

4.1.3.3 3rd fit function

Finally, as a different way of allowing the non-unidirectional flow to have an exponential dependence on Pe of less than 2, the third fit function (see Figure 4-5) is a polynomial expansion in Pe:

$$D_L^* = 1 + \frac{\mathrm{Pe}}{\alpha_{3,1}} + \frac{\mathrm{Pe}^2}{\alpha_{3,2}}. \tag{4.6}$$

Although this form of dispersion behavior does not appear in the literature, like Equation 4.5, it allows for a weaker Pe-dependence at lower values of Pe, but as suggested by Edwards et al. [23], forces $D_L^* \sim \mathrm{Pe}^2$ as $\mathrm{Pe} \to \infty$ (see Figure 4-6). It is expected that as m and dispersion increase, both parameters $\alpha_{3,i}$ decrease. This behavior is supported by the results in Table 4.1. The relatively low values of χ_3^2 indicate that this Equation 4.6 provides a better description of the results than either Equation 4.4 or 4.5. As with the parameter $\sqrt{\alpha_1}$, $\sqrt{\alpha_{3,2}}$ begins to rise at the largest values of m (see Table 4.1).

4.1.4 Critical Péclet numbers

Each of the fit equations can be manipulated to find critical values of the Péclet number Pe_c at which the behavior of the dispersion changes. For Equations 4.4 and 4.5, Pe_c is the $\sqrt[n_i]{\alpha_i}$ where n_i (either 2 or n_2) is the exponent on the Péclet number[5]. When $\mathrm{Pe} \ll \mathrm{Pe}_c$, $D_L^* \approx 1$, but when $\mathrm{Pe} \gg \mathrm{Pe}_c$, $D_L^* \approx \frac{\mathrm{Pe}^{n_i}}{\alpha_i}$.

The presence of three terms in Equation 4.6 allows for three values of $\mathrm{Pe}_{c,ij}$. The comparison of the first ($O[\mathrm{Pe}^0]$) and second ($O[\mathrm{Pe}^1]$) terms give $\mathrm{Pe}_{c,01}$ and so on:

$$\mathrm{Pe}_{c,01} \equiv \alpha_{3,1}, \tag{4.7a}$$

$$\mathrm{Pe}_{c,02} \equiv \sqrt{\alpha_{3,2}}, \tag{4.7b}$$

$$\mathrm{Pe}_{c,12} \equiv \frac{\alpha_{3,2}}{\alpha_{3,1}}, \tag{4.7c}$$

When Pe is much less than both $\mathrm{Pe}_{c,01}$ and $\mathrm{Pe}_{c,02}$, $D_L^* \approx 1$ and when Pe is much greater than $\mathrm{Pe}_{c,12}$, $D_L^* \approx \frac{\mathrm{Pe}^2}{\alpha_{3,2}}$. The condition $\mathrm{Pe}_{c,01} \ll \mathrm{Pe} \ll \mathrm{Pe}_{c,12}$ implies the presence of a distinct region in which $D_L^* \approx \frac{\mathrm{Pe}}{\alpha_{3,1}}$. This phenomenon can be observed in Figure 4-6. In this geometry, the region between $\mathrm{Pe}_{c,01} = 9$ and $\mathrm{Pe}_{c,12} = 312$ has a slope near one compared to the region above $\mathrm{Pe}_{c,12}$ where the slope is closer to two. Extreme values of $\mathrm{Pe}_{c,12}$ can prevent the $D_L^* \approx \frac{\mathrm{Pe}^2}{\alpha_{3,2}}$ dependence from being observed using the given range of Pe. The other extreme has $\mathrm{Pe}_{c,01}$ much greater than both $\mathrm{Pe}_{c,02}$ and $\mathrm{Pe}_{c,12}$, in which case the component of dispersion proportional to Pe can be ignored. In

[5] This is similar to Taylor's Péclet number limit in Equation 1.4 [12].

most geometries, the values of $\mathrm{Pe}_{c,ij}$ are too close to exactly meet these criteria, the results clearly show that at small m, the component of dispersion proportional to Pe is less important than the component proportional to Pe^2.

4.2 Collapsing results

The above procedure was completed for in-line and staggered diamond, circle, and square post arrays and in-phase and out-of-phase sinusoidal and sawtooth capillary geometries at several values of m (see Figures 2-1 and 2-2 and also Appendix B). Attempts were made to find correlations between dispersion behavior and geometry and these are tabulated in Appendix C. The non-dimensional scale m is size of the post (diamond height, circle radius, square height) or the magnitude of the sinusoid or sawtooth shape in the capillary (see Figure 4-1). The non-dimensional area A is the area of the periodic domain Ω

$$A = \int_0^1 \left[f_{\mathrm{top}}(x) - f_{\mathrm{bot}}(x) \right] \mathrm{d}x. \tag{4.8}$$

The scale $(1 - A)$ scales simply with m and only depends on the geometry of the domain, not the flow field characteristics. This does not allow for any difference between in-line and staggered post arrays or in-phase and out-of-phase capillaries. However, Johnson et al. [53, 54] suggests a scale Λ that depends on the flow field and represents pore size in a porous medium:

$$\Lambda = \frac{2 \int_A |\boldsymbol{u}|^2 \mathrm{d}A}{\int_p |\boldsymbol{u}|^2 \mathrm{d}p}, \tag{4.9}$$

where p is the wetted perimeter of the periodic domain. Using relations developed in Section 2.2 and the definition of the Jacobian to scale differential volumes between variable spaces ($\mathrm{d}x\mathrm{d}y = J\mathrm{d}\phi\mathrm{d}\psi$),

$$\Lambda = \frac{2Q}{\int_p \frac{\mathrm{d}\phi}{\sqrt{J}}}. \tag{4.10}$$

Plots of D_{L0} and the fit parameters versus these non-dimensional scales are shown in Figures 4-7 and 4-8 and Appendix D. The post arrays are represented by points *not* connected by dashed lines with diamonds, circles, and squares representing their respective post shapes. Points representing in-line and in-phase geometries are filled in. Sinusoidal capillaries are represented by diamonds. Sawtooth capillaries with flow fields calculated with either the block-Thomas algorithm or the Schwarz-Christoffel method are represented by circles or squares respectively. Points representing in-line geometries are filled in. Additionally, parameters for capillary geometries are connected

by dashed lines to distinguish them from post array parameters[6].

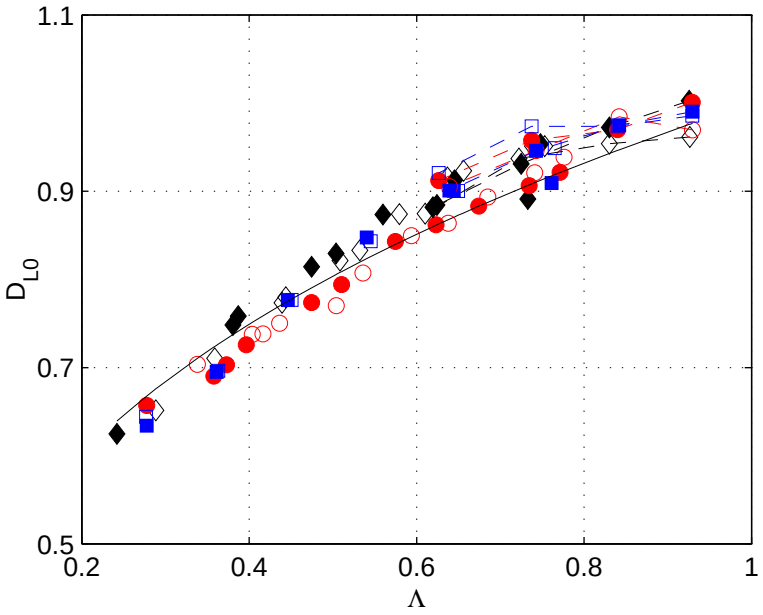

Figure 4-7: Dispersion at Pe = 0 correlated by $D_{L0} = \Lambda^{0.32}$.

When plotted against m or $(1 - A)$, the data collapse to two curves, one for post arrays and another for capillary geometries (see Figures D-3(a)–D-3(b)). In particular, the scale $(1 - A)$ has much overlap between post array and capillary geometries and thus makes a poor correlating variable. The scale m shows some continuity between post array and capillary geometries and for its simplicity does surprisingly well to collapse the results. However, as mentioned above, these parameters fail to distinguish between in-line and staggered or in-phase and out-of-phase geometries.

The scale $(1 - \Lambda)$ collapses the results for α_i better than the other scales and has different values for in-line and staggered geometries[7]. This is particularly helpful for the parameter $\alpha_{3,1}$, as it shows a significant increase from in-line to staggered geometries, especially at high m (see Appendix C)[8]. The difference between values of Λ for in-line versus staggered geometries seems to account for much of the difference in $\alpha_{3,1}$ (compare Figure 4-9(a) to Figure 4-9(b)).

The higher dispersion seen in in-line versus staggered post array geometries and in out-of-phase versus in-phase capillary geometries can be explained by considering differences in the flow field of capillary geometries. The in-phase domain shown in Figure B-9(b) has a flow field that convects

[6]For the in-phase sinusoidal capillary geometry at $m = 0.03$, the value of $\alpha_{3,1}$ is much larger than any other values of $\alpha_{3,1}$ and was considered an outlier and excluded from the plots in Figures D-3.

[7]In-phase and out-of-phase capillaries also have different Λ values, but the difference is small.

[8]The parameters α_1, α_2, and $\alpha 3, 2$ show slight increases between staggered and in-line post array geometries.

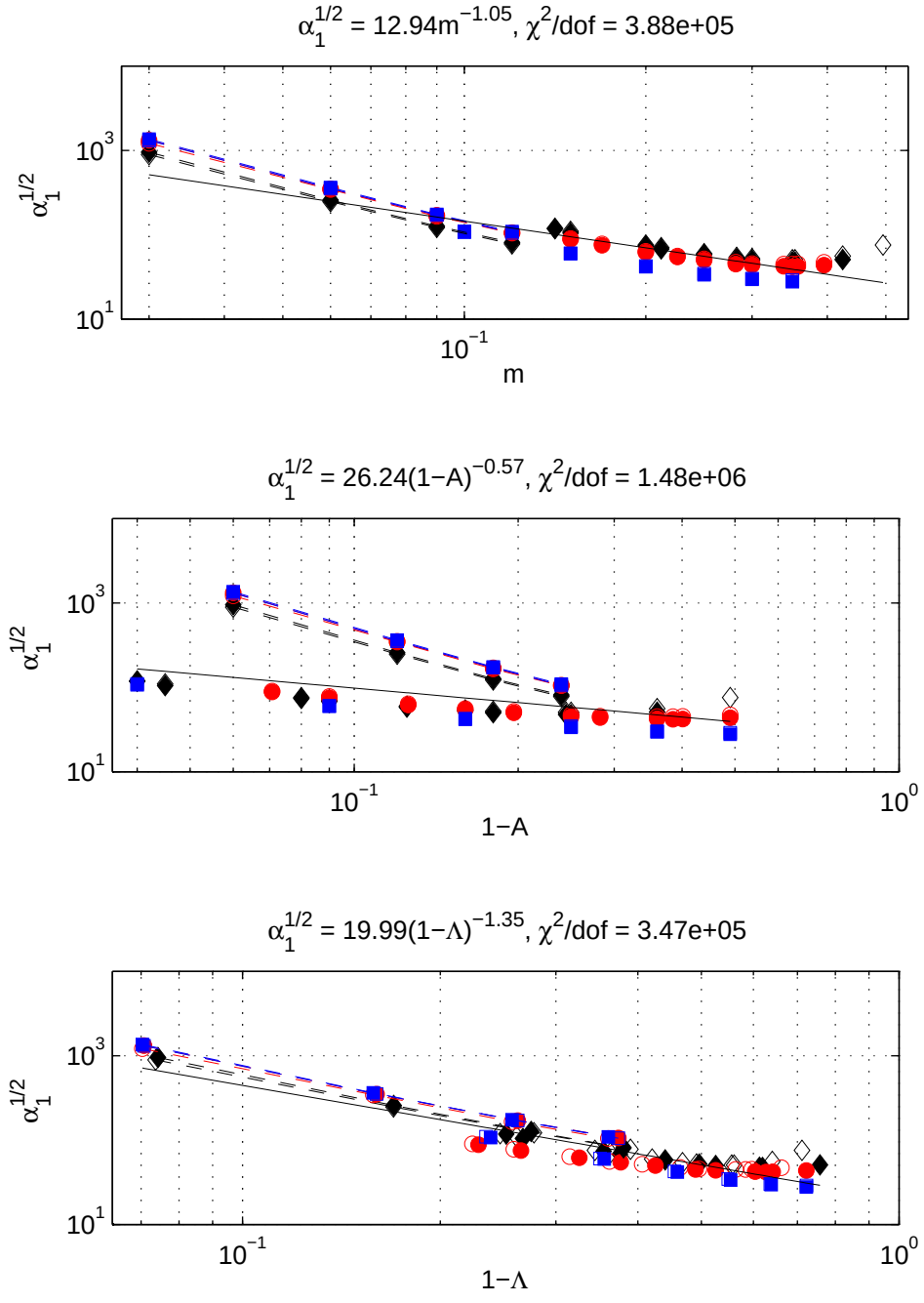

Figure 4-8: Plot of α_1 versus various geometrical parameters.

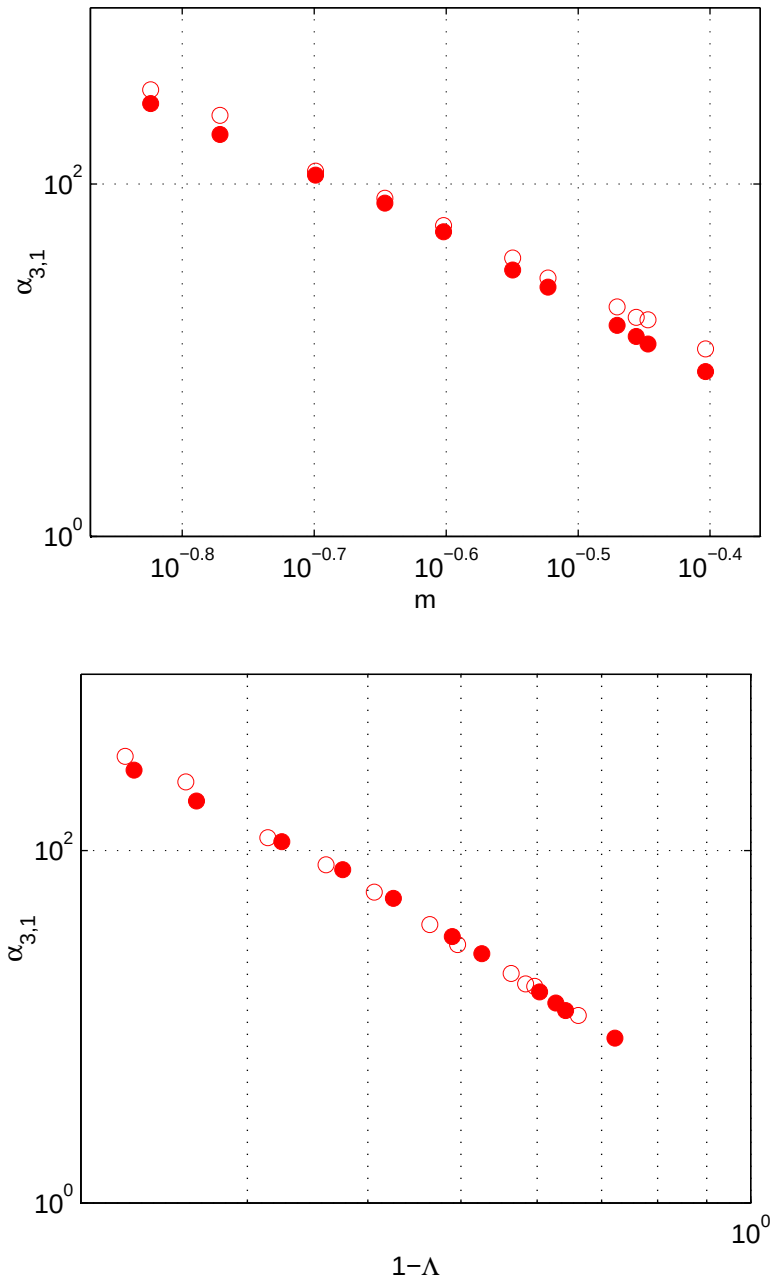

Figure 4-9: The scale m does not distinguish between values of $\alpha_{3,1}$ for in-line and staggered post arrays. The results collapse well when plotted against $(1 - \Lambda)$ however.

solute up and down as the mean velocity flows from left to right. The flow from the corresponding out-of-phase domain (Figure B-10(b)) convects solute near the top of the channel down and then up while the solute on the bottom moves exactly out of phase – up and then down. On scales smaller than the periodic domain, the in-phase (or staggered) domains have a more unidirectional character and thus have relatively stronger proportionality to Pe^2 than the out-of-phase (or in-line) domains. Eidsath et al. [24] found that in-line arrays are the highest dispersion geometrical configuration for a given interstitial volume when compared to both staggered and random arrays.

Table 4.2 shows the individual correlations for D_{L0}, $\alpha_{3,1}$, and $\sqrt{\alpha_{3,2}}$ versus $(1-\Lambda)$ for each post array and capillary geometry. These correlations can be used in Equation 4.6 to predict longitudinal dispersion given Λ and Pe. When correlations for individual geometries are used, the predictions are within a factor of two for all but one geometry: the staggered diamond post array at $m = 0.49$. Dispersion in geometries for which there is no correlation function can be predicted using the set of correlations found for all the geometries together found in the last line of Table 4.2. These correlations predict all simulation results within a factor of two except in the following geometries: in-line diamond post arrays at $m = 0.42$, staggered diamond post arrays at $m = 0.42$ and 0.49, and both in-line and staggered circle post arrays at $m = 0.39$.

Table 4.2: Correlations used to predict dispersion according to Equation 4.6.

Geometry	D_{L0}	$\alpha_{3,1}$	$\sqrt{\alpha_{3,2}}$
Diamonds	$\Lambda^{0.30}$	$8.17(1-\Lambda)^{-3.21}$	$38.21(1-\Lambda)^{-0.71}$
Circles	$\Lambda^{0.34}$	$3.98(1-\Lambda)^{-2.97}$	$36.50(1-\Lambda)^{-0.55}$
Squares	$\Lambda^{0.33}$	$2.23(1-\Lambda)^{-3.82}$	$19.61(1-\Lambda)^{-1.16}$
Sinusoidal	$\Lambda^{0.24}$	$6.97(1-\Lambda)^{-2.90}$	$19.53(1-\Lambda)^{-1.50}$
Sawtooth (BT)	$\Lambda^{0.19}$	$8.66(1-\Lambda)^{-3.09}$	$24.57(1-\Lambda)^{-1.47}$
Sawtooth (SC)	$\Lambda^{0.18}$	$14.02(1-\Lambda)^{-2.77}$	$24.58(1-\Lambda)^{-1.49}$
Total	$\Lambda^{0.32}$	$7.01(1-\Lambda)^{-3.04}$	$18.53(1-\Lambda)^{-1.51}$

4.3 Comparison with prior results

The literature contains numerous examples of numerical solutions to dispersion induced by pressure-driven flow in spatially-periodic media. Edwards et al. [23] uses the method derived by Brenner [21] to solve for dispersion in circular post arrays and contrast their results with those from Eidsath et al. [24]. Blom et al. [55] presents results of both simulations and experiments for a variety of in-line square post arrays.

4.3.1 Pure diffusion

Edwards et al. [23] gives values for longitudinal dispersion in the limit of pure diffusion (Pe = 0, see Figure 4-10) for two in-line circular post arrays and one staggered circular post array. The current results are in agreement (see Table 4.3).

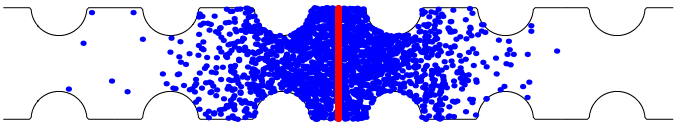

Figure 4-10: Particle distribution at $t = 0.2$ with no convection (Pe = 0) in an in-line circular post array geometry with $m = 0.25$. The red line indicates the original positions of the particles.

Table 4.3: Comparison of current results for longitudinal dispersion at Pe = 0 for circular post arrays against those in Edwards et al.

m	D_{L0} (Current results)	D_{L0} (Edwards et al. [23])	$\%_{\text{diff}}$
0.250[a]	0.8430	0.8357	0.866
0.357[a]	0.6903	0.7095	-2.781
0.357[b]	0.7376	0.7085	3.945

[a] In-line array.
[b] Staggered array.

4.3.2 Dispersion in pressure-driven flow

Edwards et al. [23] also calculated values for longitudinal dispersion at various values of Pe and look for correlations of the form

$$D_L^* = \frac{\text{Pe}^n}{\alpha}. \tag{4.11}$$

To make a comparison with the values in this thesis, the numerical results from Edwards et al. [23] were fit with Equation 4.5. In addition, Edwards et al. defines the Péclet number as $\text{Pe} \equiv \frac{2r\bar{u}}{D_{12}}$, where r is the circle radius. Thus, the Péclet values from Edwards et al. are redefined

$$\text{Pe}_e = \text{Pe} \cdot \frac{A}{2rQ}, \tag{4.12}$$

where $\bar{u} = \frac{Q}{A}$ is the mean potential flow velocity. The resulting fit parameters are shown in Table 4.4. Clearly, dispersion is higher in the pressure-driven flow case as indicated by the lower values of α_e. The numerical values used to find the results in Table 4.4 are shown in Figure 4-11.

Table 4.4: Comparison of fit parameters for potential flow and pressure-driven flow in circular post arrays. The data from Edwards et al. are denoted by subscript e.

m	$\sqrt[n_2]{\alpha_2}$	n_2	$\sqrt[n_e]{\alpha_e}$	n_e
0.250[a]	43	1.892	8	1.765
0.357[a]	21	1.606	6	1.812
0.357[b]	26	1.665	20	1.902

[a] In-line array.
[b] Staggered array.

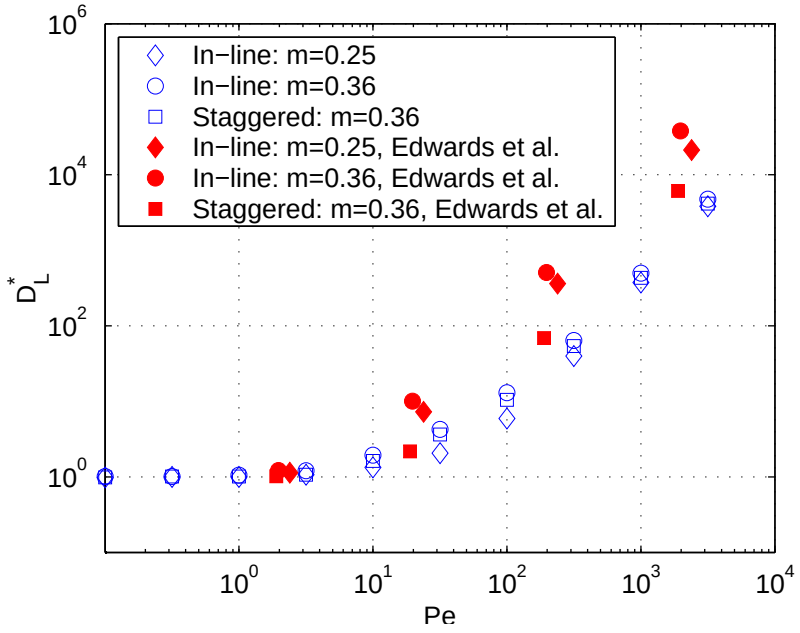

Figure 4-11: Comparison of dispersion in circular post arrays with Edwards et al. with Pe scaled as in Equation 4.12.

4.3.2.1 Application to HPLC vs. CEC

Dispersion in pressure-driven versus electrokinetically driven flow can have a major impact on the performace of High-performance Liquid Chromatography versus Capillary Electrochromatography systems. As a general rule, HPLC systems operate at Pe $\approx$ 10. Dispersion is minimized when the packed bead pore-size is constant, but packing errors can lead to irregularities. For example, a dislocation in the packing may lead to one pore having twice the diameter of the other pores. In pressure-driven flow, this will cause a four-fold increase in velocity leading to an eight-fold increase in Péclet number. Using the values for the results from Edwards et al. for an in-line circular post arrays with $m = 0.25$ in Table 4.4, $D_L^* = 2.48$ at Pe $= 10$ and $D_L^* = 59.21$ at Pe $= 80$. In contrast, a doubling of diameter does not directly scale the velocity in electroosmotic flow, so the Péclet number only doubles. Again using the current results from Table 4.4, $D_L^* = 1.06$ at Pe $= 10$ and $D_L^* = 1.24$ at Pe $= 20$. Although this is a simplified example, it is clear that dispersion may be minimized in CEC compared to HPLC systems.

4.3.3 Dispersion in potential flow

Blom et al. [55] performed simulations and experiments to measure dispersion in a variety of square post array and sawtooth capillary geometries. Values of Λ calculated from the flow field and used to calculate α_1 according to correlations similar to those in Table 4.2. Initial observations indicate that results for the square post array agree within a factor of two. However, results for the sawtooth capillary are off by over an order of magnitude.

Chapter 5

Conclusions & future work

5.1 Summary

Potential flow fields for several spatially-periodic geometries were calculated in a periodic domain using either a finite difference method in (ϕ, ψ)-space or a Schwarz-Christoffel solver. These flow fields along with a split-step Monte Carlo method were used to model a non-reacting convection-diffusion process at various values of the Péclet number between 10^{-1} and $10^{3.5}$. Particle tracking was done in (ϕ, ψ)-space to prevent artificial diffusion transverse to streamlines caused by errors in velocity field interpolation. Also, because the domain takes a rectangular shape in (ϕ, ψ)-space, the condition of zero transport across the top and bottom boundary is simpler to enforce than in physical space.

Longitudinal dispersion was calculated based on the variance of the particle distribution in the direction of the mean flow. The results were fit by three functions of the Péclet number and the free parameters calculated using the method of maximum likelihood. The third fit function, a two-term expansion in Pe, predicts the data best for almost all geometries. The goodness of fit is quantified using χ^2 values. The dependence of the numerical results on Pe is described in terms of critical Péclet numbers which depend on the calculated fit parameters. The values of Pe_c describe regimes of diffusion dominance versus convection dominance.

To collapse the fit parameters, they were plotted agains various non-dimensional scales: the vertical scale of the geometric obstruction m, the solid non-dimensional area of the periodic domain $(1 - A)$, and one minus the pore size $(1 - \Lambda)$. The scales m and $(1 - A)$ do not distinguish in-line from staggered or in-phase from out-of-phase geometries and thus cannot completely collapse the values of the fit parameters. The scale $(1 - \Lambda)$ does make this distinction and correlates the data well

based on exponential fits. Using the correlations found for D_{L0}, $\alpha_{3,1}$, and $\alpha_{3,2}$, a set of relations are found that predict longitudinal dispersion for individual geometries and also a relation that predicts longitudinal dispersion in a general periodic geometry as a function of Λ and Pe

$$D_L = \Lambda^{0.32}\left[1 + \frac{\mathrm{Pe}}{7.01(1-\Lambda)^{-3.04}} + \frac{\mathrm{Pe}^2}{343.36(1-\Lambda)^{-3.02}}\right]. \tag{5.1}$$

Finally, some results from the literature for simulations of dispersion in pressure-driven flow were compared to the current results and found to be higher for equivalent geometries after scaling for different definitions of the Péclet number. In addition, simulation and experimental results for dispersion in potential flow in the literature were compared to current results and found to differ by a factor of two for some cases, but over an order of magnitude in others.

5.2 Impact

These results can be used by members of the analytical chemistry community to select chromatography geometries that meet requirements for resolution while providing the necessary surface area to drive separation. The analysis of fit parameters provides a means of understanding the dispersive effects of different geometries based on the scale $(1-\Lambda)$. The collapse of data along $(1-\Lambda)$ indicates that dispersion in electrokinetic flow can be accurately predicted for a given geometry with knowlege of the interstitial flow field. The current results also indicate that even in geometries where the potential flow has high gradients, dispersion is much lower than for pressure-driven flow in the same geometries. This may be an advantage for Capillary Electrophoresis systems compared to High-performance Liquid chromatography systems.

5.3 Future work

The computer routines written for this research will continue to be used to simulate dispersion for further refinement of the current results. In addition, the routines can be altered to isolate particular physical attributes of dispersion. As an example, the streamwise diffusion can be selectively turned off to determine its importance[1] [8]. This may allow insight into the mechanisms of dispersion in spatially-periodic media.

The numerical results presented in this thesis only describe the fully-developed late-time dispersion. However, the variance of the solute distribution is calculated at both early and late times.

[1] Taylor [11] ignored axial diffusion $\left(\frac{\partial c}{\partial x}\right)$ in his analysis.

Because microfluidic systems often transport solutes short distances, early-time dispersion is of interest and will be studied. Calculation of dispersion at early times cannot be done with analytical methods such as that developed by Brenner [21] and is another benefit of the particle tracking method.

Finally, the simple functional form of the sinusoidal boundaries lends itself to a perturbation analysis of Brenner's method (Equation 1.12) around small m. Potential flow fields can also be calculated for sinusoidal domains of small aspect ratio ($\frac{h}{\lambda} \ll 1$). The dispersion simulations in these geometries can be compared to a lubrication approximation and contrasted with the results for pressure-driven flow in sinusoidal capillaries from Hoagland et al. [22].

Appendix A

Tables of flowrates

The following tables (Tables A.1–A.6) list flowrates for each domain at Pe = 1. The first flowrate $Q_\psi = \psi_{top}$ is simply the upper limit of the domain in (ϕ, ψ)-space. The second flowrate Q_u is the average of the flowrate at the inlet, middle, and outlet of the domain

$$Q_u = \frac{1}{3}\left[\int_{f_{bot}(0)}^{f_{top}(0)} u(0,y)\ \mathrm{d}y + \int_{f_{bot}(\frac{1}{2})}^{f_{top}(\frac{1}{2})} u\left(\frac{1}{2},y\right)\ \mathrm{d}y + \int_{f_{bot}(1)}^{f_{top}(1)} u(1,y)\ \mathrm{d}y\right]. \tag{A.1}$$

A.1 Post arrays

Table A.1: Flowrate: Diamonds.

m	A^{a}	Q_ψ	Q_u	$\%_{\text{diff}}$
0.141	0.960	0.916	0.916	0.002
0.150	0.955	0.906	0.906	0.002
0.200	0.920	0.839	0.839	-0.002
0.212	0.910	0.820	0.820	-0.003
0.250	0.875	0.758	0.758	-0.007
0.283	0.840	0.699	0.699	-0.011
0.300	0.820	0.667	0.667	-0.013
0.350	0.755	0.568	0.568	-0.020
0.354	0.750	0.561	0.561	-0.021
0.424	0.640	0.405	0.405	-0.020

[a] $A = 1 - 2m^2$

(a) In-line

m	A^{a}	Q_ψ	Q_u	$\%_{\text{diff}}$
0.141	0.960	0.916	0.916	-0.078
0.150	0.955	0.907	0.906	-0.079
0.200	0.920	0.840	0.839	-0.088
0.212	0.910	0.822	0.821	-0.091
0.250	0.875	0.762	0.761	-0.100
0.283	0.840	0.706	0.705	-0.110
0.300	0.820	0.675	0.674	-0.116
0.350	0.755	0.584	0.584	-0.136
0.354	0.750	0.578	0.577	-0.137
0.424	0.640	0.449	0.448	-0.174
0.495	0.510	0.328	0.331	1.029

[a] $A = 1 - 2m^2$

(b) Staggered

Table A.2: Flowrate: Circles.

m	A^{a}	Q_ψ	Q_u	$\%_{\mathrm{diff}}$
0.150	0.929	0.868	0.868	-0.002
0.169	0.910	0.835	0.835	-0.003
0.200	0.874	0.777	0.777	-0.003
0.226	0.840	0.724	0.724	-0.003
0.250	0.804	0.672	0.672	-0.002
0.282	0.750	0.600	0.600	-0.001
0.300	0.717	0.559	0.559	0.001
0.339	0.640	0.469	0.469	0.014
0.350	0.615	0.442	0.442	0.024
0.357	0.599	0.425	0.425	0.035
0.395	0.510	0.335	0.336	0.327

[a] $A = 1 - \pi m^2$

(a) In-line

m	A^{a}	Q_ψ	Q_u	$\%_{\mathrm{diff}}$
0.150	0.929	0.869	0.869	-0.013
0.169	0.910	0.836	0.836	-0.013
0.200	0.874	0.779	0.779	-0.014
0.226	0.840	0.728	0.728	-0.015
0.250	0.804	0.677	0.677	-0.016
0.282	0.750	0.608	0.608	-0.017
0.300	0.717	0.569	0.568	-0.017
0.339	0.640	0.484	0.484	-0.014
0.350	0.615	0.458	0.458	-0.011
0.357	0.599	0.443	0.443	-0.008
0.395	0.510	0.361	0.362	0.074

[a] $A = 1 - \pi m^2$

(b) Staggered

Table A.3: Flowrate: Squares.

m	A^{a}	Q_ψ	Q_u	$\%_{\mathrm{diff}}$
0.100	0.960	0.916	0.916	0.000
0.150	0.910	0.821	0.821	0.000
0.200	0.840	0.704	0.704	0.001
0.250	0.750	0.577	0.577	0.006
0.300	0.640	0.450	0.450	0.041
0.350	0.510	0.327	0.329	0.627

[a] $A = 1 - 4m^2$

(a) In-line

m	A^{a}	Q_ψ	Q_u	$\%_{\mathrm{diff}}$
0.100	0.960	0.916	0.916	0.000
0.150	0.910	0.822	0.822	0.000
0.200	0.840	0.707	0.707	0.001
0.250	0.750	0.581	0.581	0.004
0.300	0.640	0.454	0.454	0.020
0.350	0.510	0.330	0.331	0.271

[a] $A = 1 - 4m^2$

(b) Staggered

A.2 Capillaries

Table A.4: Flowrate: Sinusoidal.

m	A^{a}	Q_ψ	Q_u	$\%_{\text{diff}}$
0.030	0.940	0.934	0.934	0.051
0.060	0.880	0.857	0.858	0.078
0.090	0.820	0.772	0.772	0.081
0.120	0.760	0.679	0.680	0.047

[a] $A = 1 - 2m$

(a) In-phase

m	A^{a}	Q_ψ	Q_u	$\%_{\text{diff}}$
0.030	0.940	0.935	0.934	-0.083
0.060	0.880	0.859	0.857	-0.211
0.090	0.820	0.774	0.771	-0.420
0.120	0.760	0.681	0.676	-0.792

[a] $A = 1 - 2m$

(b) Out-of-phase

Table A.5: Flowrate: Sawtooth (flow field calculated with block-Thomas algorithm).

m	A^{a}	Q_ψ	Q_u	$\%_{\text{diff}}$
0.030	0.940	0.935	0.936	0.148
0.060	0.880	0.862	0.864	0.226
0.090	0.820	0.784	0.786	0.256
0.120	0.760	0.699	0.701	0.258

[a] $A = 1 - 2m$

(a) In-phase

m	A^{a}	Q_ψ	Q_u	$\%_{\text{diff}}$
0.030	0.940	0.938	0.935	-0.331
0.060	0.880	0.870	0.863	-0.883
0.090	0.820	0.797	0.782	-1.880
0.120	0.760	0.721	0.694	-3.794

[a] $A = 1 - 2m$

(b) Out-of-phase

Table A.6: Flowrate: Sawtooth (flow field calculated with Schwarz-Christoffel method).

m	A^{a}	Q_ψ	Q_u	$\%_{\mathrm{diff}}$
0.030	0.940	0.936	0.936	0.010
0.060	0.880	0.865	0.865	0.040
0.090	0.820	0.786	0.787	0.088
0.120	0.760	0.702	0.703	0.155

[a] $A = 1 - 2m$

(a) In-phase

m	A^{a}	Q_ψ	Q_u	$\%_{\mathrm{diff}}$
0.030	0.940	0.936	0.937	0.062
0.060	0.880	0.864	0.866	0.154
0.090	0.820	0.786	0.788	0.275
0.120	0.760	0.700	0.703	0.429

[a] $A = 1 - 2m$

(b) Out-of-phase

Appendix B

Geometries

The following figures show the periodic domains and contour plots of ϕ and ψ for the smallest and largest amplitude of each shape of post array (Figures B-1–B-6) and capillary (Figures B-7–B-12). Some geometries (for example Figure B-6(b)) have have irregular corners in concave regions. In (ϕ, ψ)-space, the numerical grid is regularly spaced, but when transformed back into (x, y)-space, the (ϕ, ψ)-grid will be densely packed in regions of high acceleration (convex regions) and sparse in regions of low acceleration (concave regions). The representation of the (ϕ, ψ)-grid in (x, y)-space will determine the resolution of the domain boundary. Thus, boundary resolution will be lost in these convex regions. Fortunately, the local value Pe is so small in these regions that these inaccuracies do not contribute greatly to the overall error.

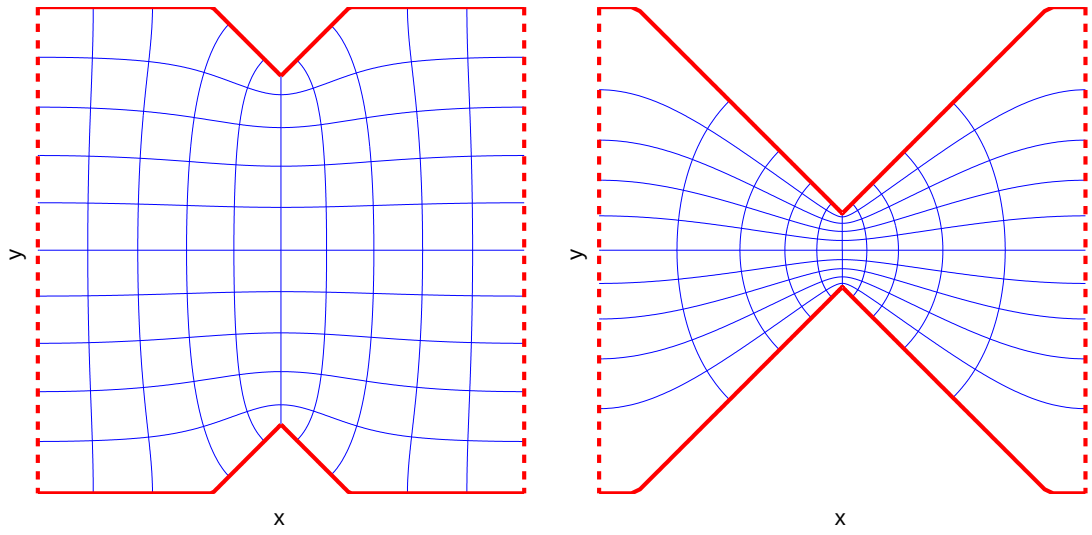

(a) (b)

Figure B-1: Unit domain: In-line diamonds; $0.1414 \leq m \leq 0.4243$.

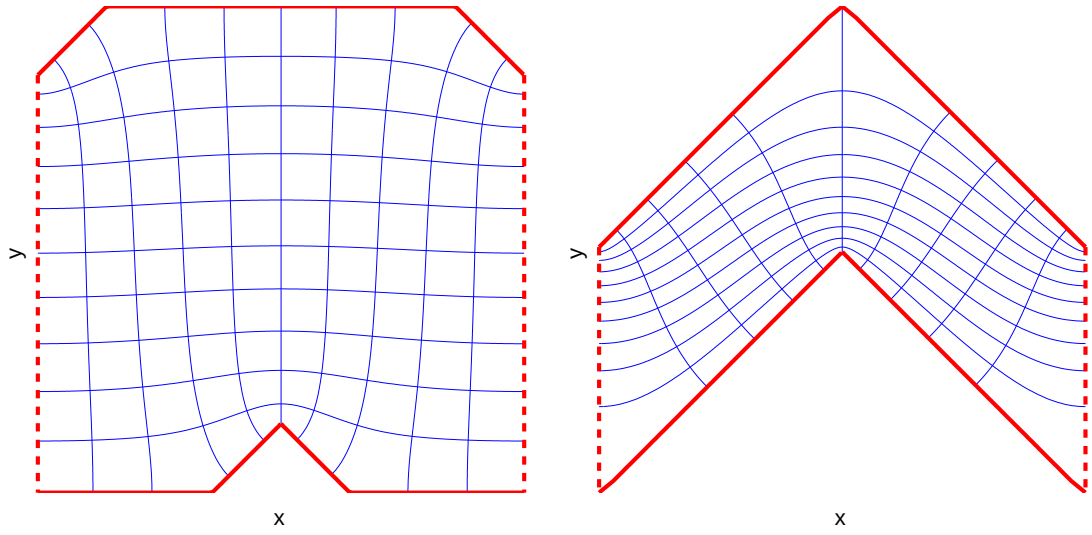

(a) (b)

Figure B-2: Unit domain: Staggered diamonds; $0.1414 \leq m \leq 0.4950$.

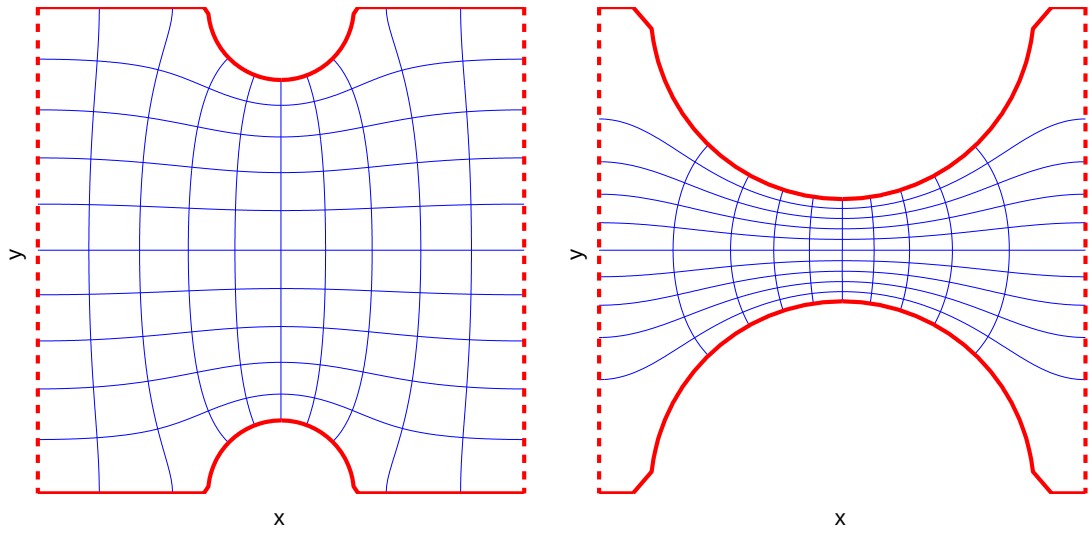

(a) (b)

Figure B-3: Unit domain: In-line circles; $0.15 \leq m \leq 0.3949$.

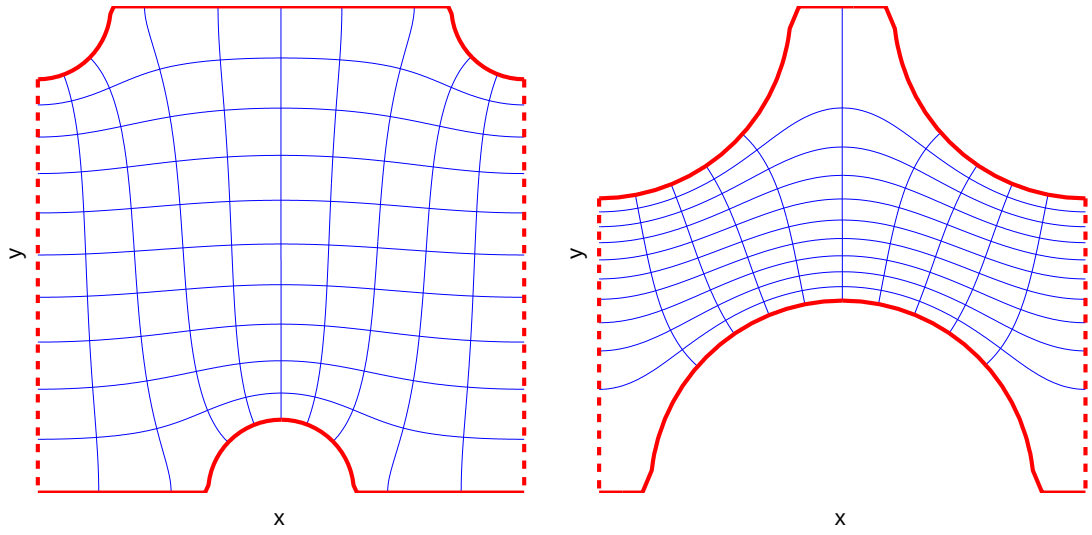

(a) (b)

Figure B-4: Unit domain: Staggered circles; $0.15 \leq m \leq 0.3949$.

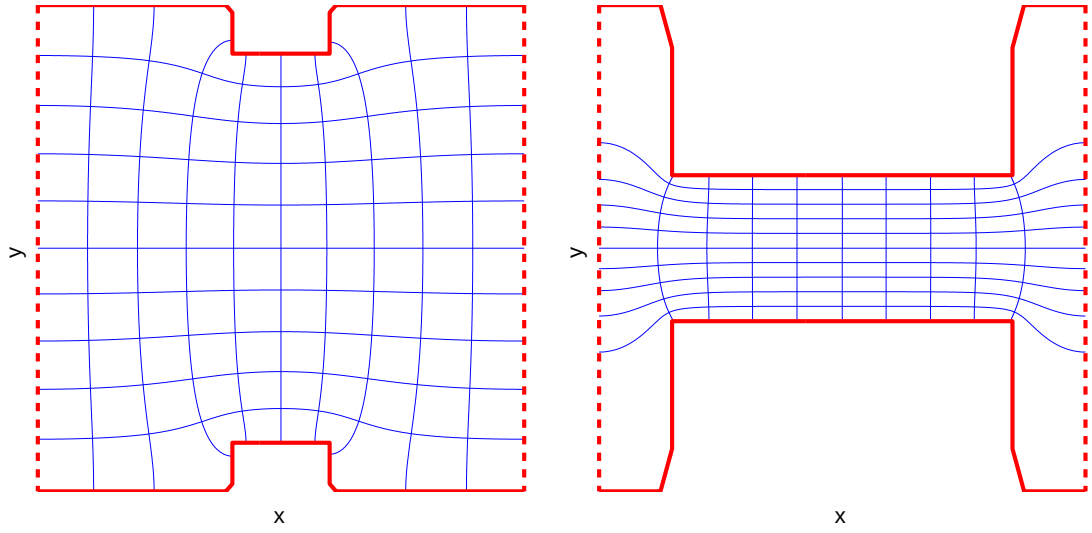

(a) (b)

Figure B-5: Unit domain: In-line squares; $0.10 \leq m \leq 0.35$.

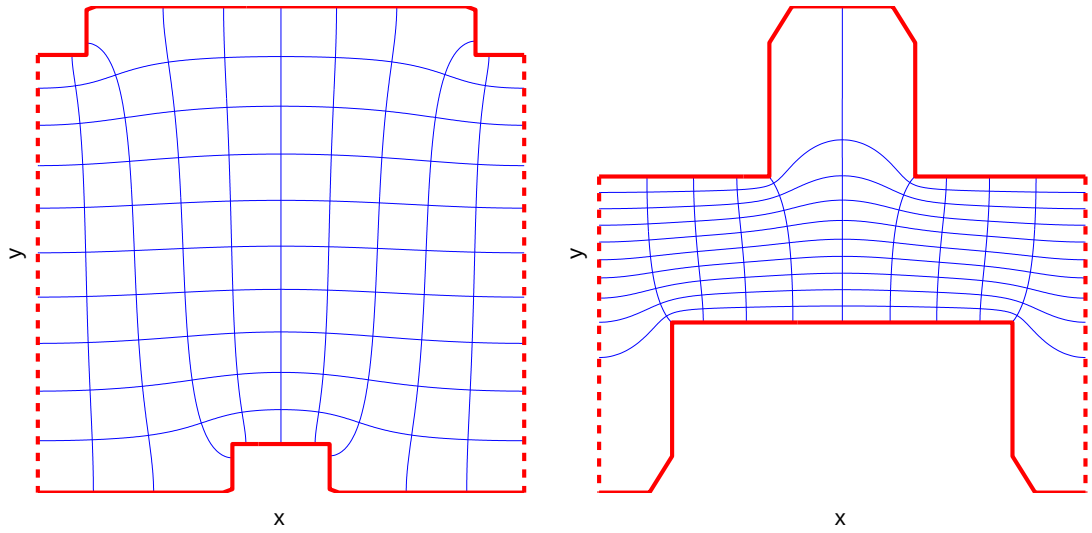

(a) (b)

Figure B-6: Unit domain: Staggered squares; $0.10 \leq m \leq 0.35$.

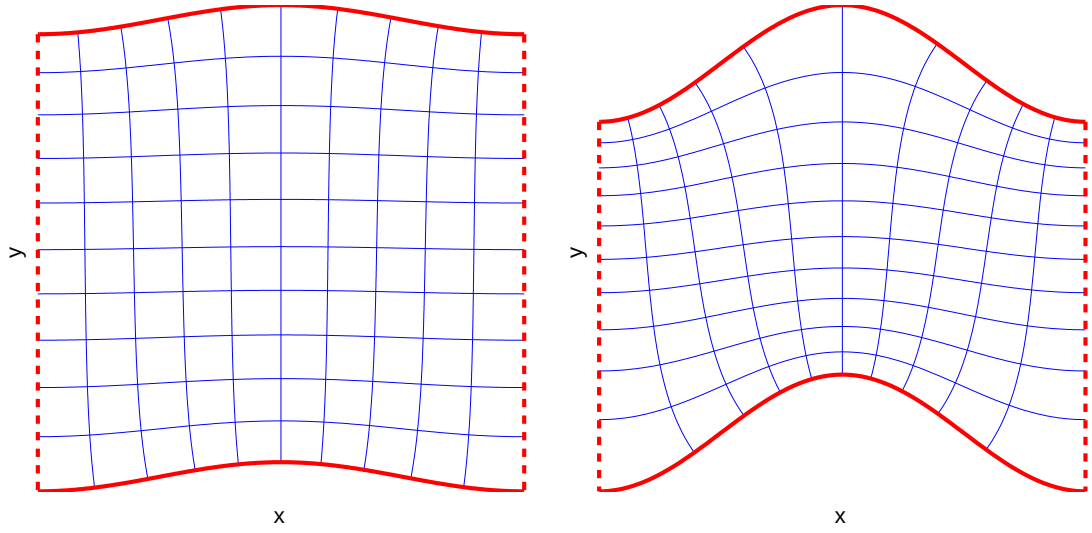

(a) (b)

Figure B-7: Unit domain: In-phase sinusoidal; $0.03 \leq m \leq 0.12$.

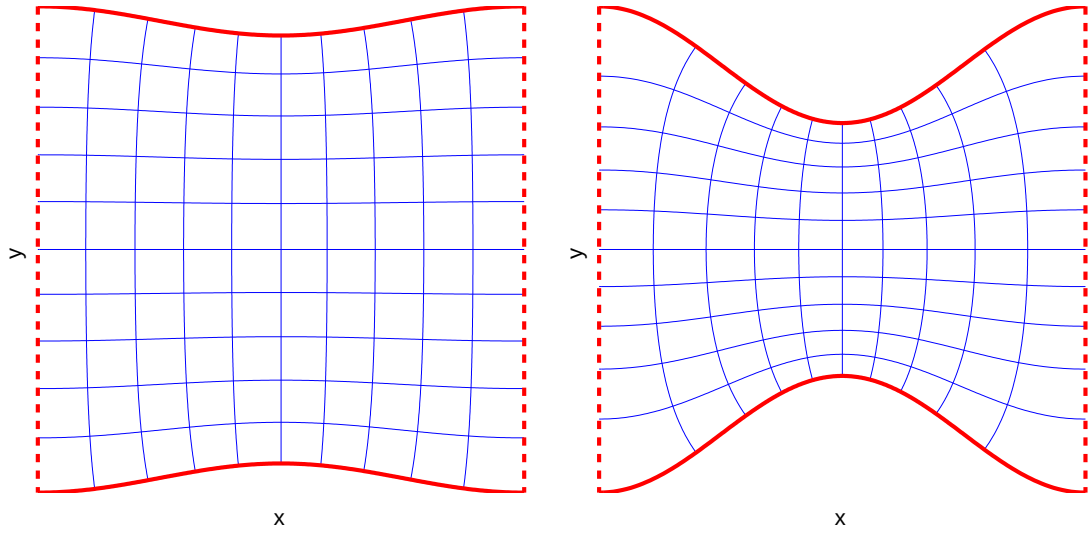

(a) (b)

Figure B-8: Unit domain: Out-of-phase sinusoidal; $0.03 \leq m \leq 0.12$.

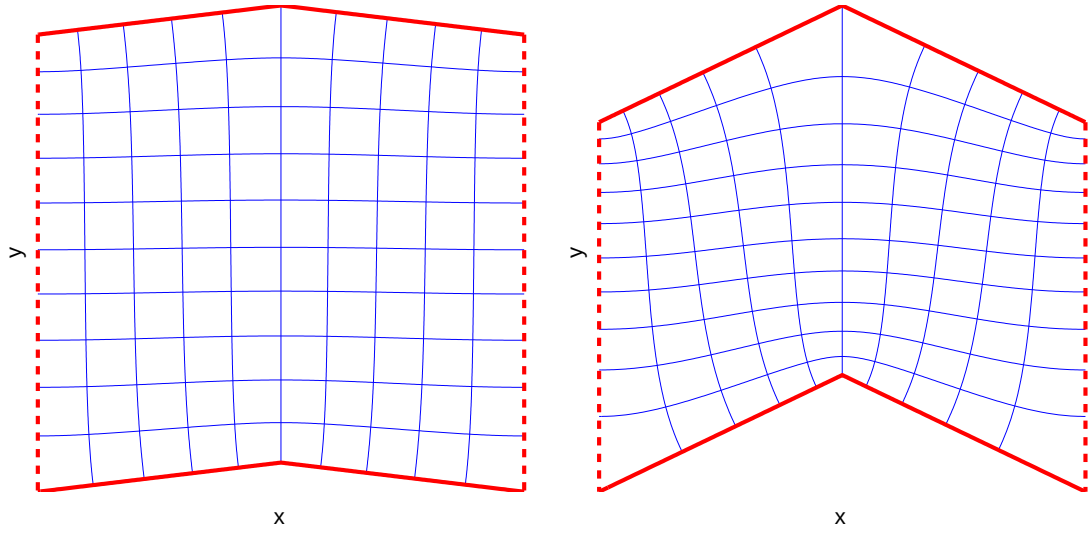

(a) (b)

Figure B-9: Unit domain: In-phase sawtooth (block-Thomas); $0.03 \leq m \leq 0.12$.

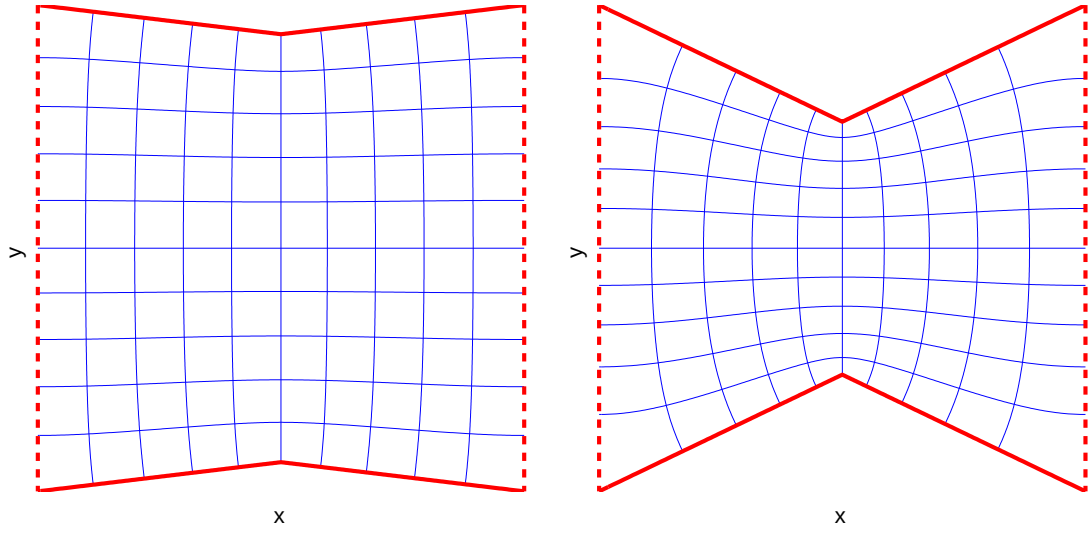

(a) (b)

Figure B-10: Unit domain: Out-of-phase sawtooth (block-Thomas); $0.03 \leq m \leq 0.12$.

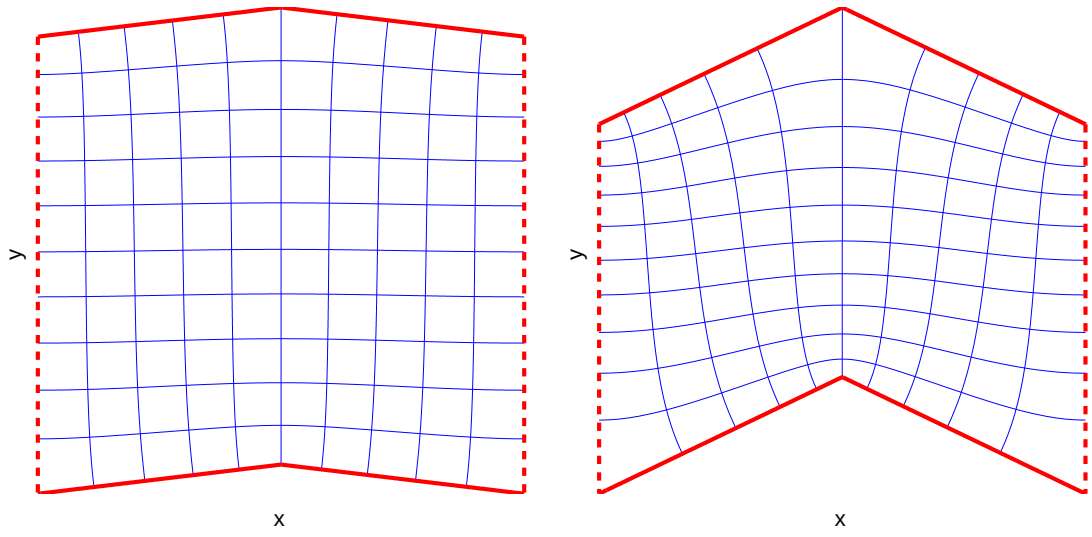

(a) (b)

Figure B-11: Unit domain: In-phase sawtooth (Schwarz-Christoffel); $0.03 \leq m \leq 0.12$.

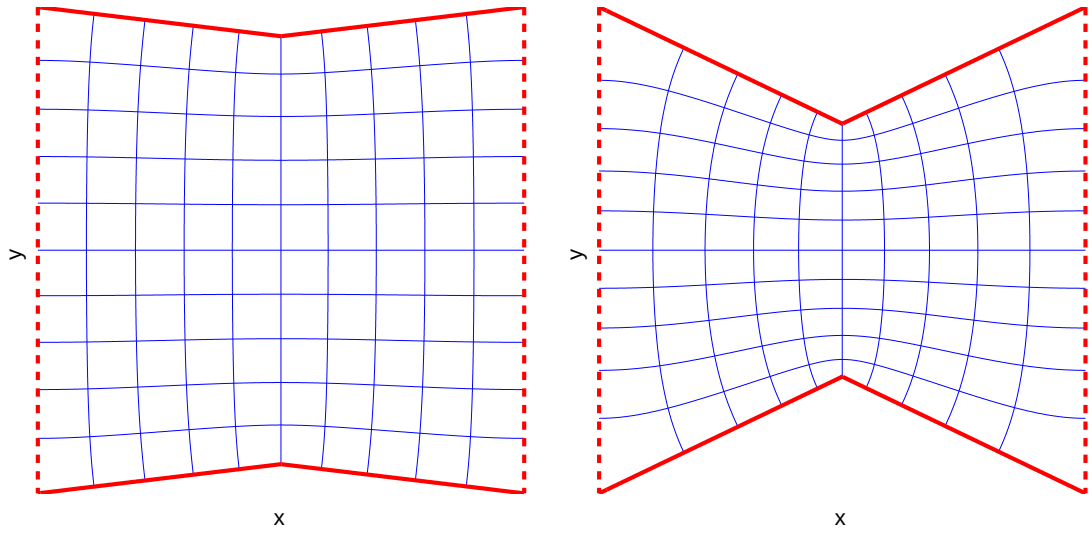

(a) (b)

Figure B-12: Unit domain: Out-of-phase sawtooth (Schwarz-Christoffel); $0.03 \leq m \leq 0.12$.

Appendix C

Tables of results

The following tables (Tables C.1–C.12) show the best fit parameters for Equations 4.4, 4.5, and 4.6. Four geometric parameters are included. For the post arrays, m is the half height of the shape (diamond, circle, or square) perpendicular to the flow. For the sinusoidal and sawtooth capillaries, m is the half-amplitude of the periodic boundary. The non-dimensional scale A is the area of the periodic domain. A characteristic non-dimensional scale Λ is defined in Equation 4.10

C.1 Post arrays

Table C.1: Results: In-line diamonds.

m	A^{a}	Λ	D_{L0}	$\sqrt{\alpha_1}$	χ_1^2	$\sqrt[n_2]{\alpha_2}$	n_2	χ_2^2	$\alpha_{3,1}$	$\sqrt{\alpha_{3,2}}$	$\frac{\alpha_{3,2}}{\alpha_{3,1}}$	χ_3^2
0.141	0.960	0.748	0.953	118	7	113	1.964	4	653	120	22	2
0.150	0.955	0.733	0.891	105	31	99	1.946	25	320	108	37	15
0.200	0.920	0.645	0.912	74	21	71	1.965	18	249	76	23	7
0.212	0.910	0.624	0.884	68	38	64	1.946	29	161	71	31	11
0.250	0.875	0.560	0.874	58	45	54	1.943	35	119	61	31	10
0.283	0.840	0.504	0.830	52	75	47	1.920	54	78	55	39	14
0.300	0.820	0.475	0.814	50	95	44	1.911	69	64	53	44	17
0.350	0.755	0.387	0.758	48	187	39	1.864	133	39	52	70	29
0.354	0.750	0.381	0.748	47	195	39	1.861	138	37	52	72	30
0.424	0.640	0.242	0.625	51	459	33	1.724	294	20	59	169	64

[a] $A = 1 - 2m^2$

Table C.2: Results: Staggered diamonds.

m	A^{a}	Λ	D_{L0}	$\sqrt{\alpha_1}$	χ_1^2	$\sqrt[n_2]{\alpha_2}$	n_2	χ_2^2	$\alpha_{3,1}$	$\sqrt{\alpha_{3,2}}$	$\frac{\alpha_{3,2}}{\alpha_{3,1}}$	χ_3^2
0.141	0.960	0.753	0.951	119	6	116	1.972	5	739	121	20	2
0.150	0.955	0.738	0.951	110	6	107	1.976	5	667	111	19	2
0.200	0.920	0.656	0.923	75	20	71	1.952	13	242	78	25	5
0.212	0.910	0.637	0.916	70	17	68	1.965	13	257	72	20	5
0.250	0.875	0.579	0.874	59	42	55	1.941	31	125	62	31	9
0.283	0.840	0.532	0.833	54	70	49	1.923	51	84	57	39	14
0.300	0.820	0.509	0.821	52	83	47	1.919	62	73	55	42	16
0.350	0.755	0.444	0.780	51	137	42	1.875	90	49	55	60	18
0.354	0.750	0.439	0.774	50	142	43	1.882	100	49	54	60	22
0.424	0.640	0.359	0.710	56	276	41	1.793	176	33	63	120	34
0.495	0.510	0.289	0.651	75	422	43	1.636	202	30	89	262	33

[a] $A = 1 - 2m^2$

Table C.3: Results: In-line circles.

m	A^{a}	Λ	D_{L0}	$\sqrt{\alpha_1}$	χ_1^2	$\sqrt[n_2]{\alpha_2}$	n_2	χ_2^2	$\alpha_{3,1}$	$\sqrt{\alpha_{3,2}}$	$\frac{\alpha_{3,2}}{\alpha_{3,1}}$	χ_3^2
0.150	0.929	0.771	0.922	88	21	84	1.955	16	286	91	29	6
0.169	0.910	0.734	0.906	75	32	71	1.947	24	191	78	32	8
0.200	0.874	0.674	0.883	62	52	56	1.928	37	112	65	37	9
0.226	0.840	0.623	0.862	55	76	49	1.912	53	78	58	43	11
0.250	0.804	0.575	0.843	50	118	43	1.892	83	54	54	53	16
0.282	0.750	0.510	0.794	45	213	36	1.847	144	32	49	75	26
0.300	0.717	0.474	0.774	44	266	33	1.808	163	26	48	91	22
0.339	0.640	0.397	0.726	42	458	25	1.692	229	16	48	148	18
0.350	0.615	0.373	0.703	42	527	22	1.640	227	14	48	171	13
0.357	0.599	0.358	0.690	42	586	21	1.606	244	12	49	193	12
0.395	0.510	0.278	0.657	44	865	14	1.454	178	9	52	312	25

[a] $A = 1 - \pi m^2$

Table C.4: Results: Staggered circles.

m	A^{a}	Λ	D_{L0}	$\sqrt{\alpha_1}$	χ_1^2	$\sqrt[n_2]{\alpha_2}$	n_2	χ_2^2	$\alpha_{3,1}$	$\sqrt{\alpha_{3,2}}$	$\frac{\alpha_{3,2}}{\alpha_{3,1}}$	χ_3^2
0.150	0.929	0.776	0.939	90	15	86	1.962	12	342	92	25	4
0.169	0.910	0.741	0.921	78	21	74	1.957	16	245	80	26	5
0.200	0.874	0.685	0.894	64	48	58	1.927	32	118	67	38	6
0.226	0.840	0.638	0.864	56	70	50	1.915	48	83	59	42	10
0.250	0.804	0.594	0.850	52	109	44	1.889	71	58	55	52	14
0.282	0.750	0.536	0.807	47	179	38	1.855	119	38	52	70	21
0.300	0.717	0.504	0.770	45	238	35	1.820	146	29	50	86	19
0.339	0.640	0.436	0.750	45	371	29	1.734	199	20	51	128	24
0.350	0.615	0.416	0.738	45	430	26	1.685	198	18	51	150	17
0.357	0.599	0.404	0.738	45	452	26	1.665	192	17	52	157	21
0.395	0.510	0.338	0.704	47	708	18	1.505	159	12	55	262	36

[a] $A = 1 - \pi m^2$

Table C.5: Results: In-line squares.

m	A^{a}	Λ	D_{L0}	$\sqrt{\alpha_1}$	χ_1^2	$\sqrt[n_2]{\alpha_2}$	n_2	χ_2^2	$\alpha_{3,1}$	$\sqrt{\alpha_{3,2}}$	$\frac{\alpha_{3,2}}{\alpha_{3,1}}$	χ_3^2
0.100	0.960	0.761	0.910	107	20	102	1.958	16	372	110	33	7
0.150	0.910	0.644	0.901	60	46	55	1.938	35	128	62	30	14
0.200	0.840	0.540	0.848	42	110	35	1.883	63	45	45	44	6
0.250	0.750	0.446	0.777	34	280	24	1.788	133	19	37	73	9
0.300	0.640	0.361	0.695	30	594	14	1.617	179	9	33	124	35
0.350	0.510	0.278	0.634	28	1090	8	1.483	56	5	31	178	272

[a] $A = 1 - 4m^2$

Table C.6: Results: Staggered squares.

m	A^{a}	Λ	D_{L0}	$\sqrt{\alpha_1}$	χ_1^2	$\sqrt[n_2]{\alpha_2}$	n_2	χ_2^2	$\alpha_{3,1}$	$\sqrt{\alpha_{3,2}}$	$\frac{\alpha_{3,2}}{\alpha_{3,1}}$	χ_3^2
0.100	0.960	0.765	0.949	109	8	107	1.981	7	613	112	20	3
0.150	0.910	0.650	0.900	60	35	55	1.932	21	130	63	30	3
0.200	0.840	0.545	0.843	42	108	36	1.888	65	47	45	44	7
0.250	0.750	0.451	0.777	34	274	24	1.789	122	20	38	73	11
0.300	0.640	0.363	0.696	30	562	15	1.636	174	10	34	119	40
0.350	0.510	0.277	0.644	29	1045	8	1.488	60	6	32	180	254

[a] $A = 1 - 4m^2$

C.2 Capillaries

Table C.7: Results: In-phase sinusoidal.

m	A^{a}	Λ	D_{L0}	$\sqrt{\alpha_1}$	χ_1^2	$\sqrt[n_2]{\alpha_2}$	n_2	χ_2^2	$\alpha_{3,1}$	$\sqrt{\alpha_{3,2}}$	$\frac{\alpha_{3,2}}{\alpha_{3,1}}$	χ_3^2
0.030	0.940	0.926	1.003	953	1	961	2.019	1	$10^{17\mathrm{b}}$	953	0	1
0.060	0.880	0.830	0.973	257	7	248	1.960	6	1437	263	48	3
0.090	0.820	0.725	0.931	126	36	117	1.928	27	294	132	60	10
0.120	0.760	0.619	0.882	81	83	72	1.901	60	115	87	65	18

[a] $A = 1 - 2m$

[b] This point was not included in the parameter plots due to its excessive size.

Table C.8: Results: Out-of-phase sinusoidal.

m	A^{a}	Λ	D_{L0}	$\sqrt{\alpha_1}$	χ_1^2	$\sqrt[n_2]{\alpha_2}$	n_2	χ_2^2	$\alpha_{3,1}$	$\sqrt{\alpha_{3,2}}$	$\frac{\alpha_{3,2}}{\alpha_{3,1}}$	χ_3^2
0.030	0.940	0.926	0.962	891	5	867	1.943	4	7080	918	119	3
0.060	0.880	0.830	0.954	247	14	236	1.949	11	1053	255	62	6
0.090	0.820	0.722	0.937	122	35	113	1.928	26	286	128	57	9
0.120	0.760	0.610	0.875	78	98	68	1.890	70	98	83	71	20

[a] $A = 1 - 2m$

Table C.9: Results: In-phase sawtooth (flow field calculated with block-Thomas algorithm).

m	A^{a}	Λ	D_{L0}	$\sqrt{\alpha_1}$	χ_1^2	$\sqrt[n_2]{\alpha_2}$	n_2	χ_2^2	$\alpha_{3,1}$	$\sqrt{\alpha_{3,2}}$	$\frac{\alpha_{3,2}}{\alpha_{3,1}}$	χ_3^2
0.030	0.940	0.929	1.001	1319	1	1298	1.954	0	28139	1337	63	1
0.060	0.880	0.840	0.970	349	7	337	1.954	5	2087	359	62	3
0.090	0.820	0.737	0.958	170	20	160	1.941	15	540	176	58	6
0.120	0.760	0.627	0.912	106	54	96	1.910	38	189	112	67	11

[a] $A = 1 - 2m$

Table C.10: Results: Out-of-phase sawtooth (flow field calculated with block-Thomas algorithm).

m	A^{a}	Λ	D_{L0}	$\sqrt{\alpha_1}$	χ_1^2	$\sqrt[n_2]{\alpha_2}$	n_2	χ_2^2	$\alpha_{3,1}$	$\sqrt{\alpha_{3,2}}$	$\frac{\alpha_{3,2}}{\alpha_{3,1}}$	χ_3^2
0.030	0.940	0.930	0.970	1215	3	1194	1.954	3	12466	1248	125	2
0.060	0.880	0.842	0.985	343	7	334	1.963	6	3187	349	38	5
0.090	0.820	0.743	0.946	165	23	156	1.944	19	522	172	56	9
0.120	0.760	0.639	0.905	105	57	94	1.906	40	183	111	67	13

[a] $A = 1 - 2m$

Table C.11: Results: In-phase sawtooth (flow field calculated with Schwarz-Christoffel method).

m	A^{a}	Λ	D_{L0}	$\sqrt{\alpha_1}$	χ_1^2	$\sqrt[n_2]{\alpha_2}$	n_2	χ_2^2	$\alpha_{3,1}$	$\sqrt{\alpha_{3,2}}$	$\frac{\alpha_{3,2}}{\alpha_{3,1}}$	χ_3^2
0.030	0.940	0.930	0.990	1358	1	1319	1.918	1	14166	1396	138	1
0.060	0.880	0.842	0.975	361	5	352	1.963	4	2581	370	53	2
0.090	0.820	0.743	0.946	174	22	164	1.945	18	558	180	58	8
0.120	0.760	0.639	0.901	109	63	98	1.905	46	181	116	74	14

[a] $A = 1 - 2m$

Table C.12: Results: Out-of-phase sawtooth (flow field calculated with Schwarz-Christoffel method).

m	A^{a}	Λ	D_{L0}	$\sqrt{\alpha_1}$	χ_1^2	$\sqrt[n_2]{\alpha_2}$	n_2	χ_2^2	$\alpha_{3,1}$	$\sqrt{\alpha_{3,2}}$	$\frac{\alpha_{3,2}}{\alpha_{3,1}}$	χ_3^2
0.030	0.940	0.929	0.986	1309	1	1292	1.963	1	20091	1333	88	1
0.060	0.880	0.840	0.974	351	8	335	1.942	5	1839	361	71	3
0.090	0.820	0.737	0.974	171	14	163	1.956	12	678	176	46	5
0.120	0.760	0.627	0.921	105	47	96	1.921	35	214	111	57	13

[a] $A = 1 - 2m$

Appendix D

Plots of collapsed results

The following figures (Figures D-1–D-4) show the free parameters from Equations 4.4 and 4.5 plotted against the non-dimensionalized scales m, $(1 - A)$, and $(1 - \Lambda)$.

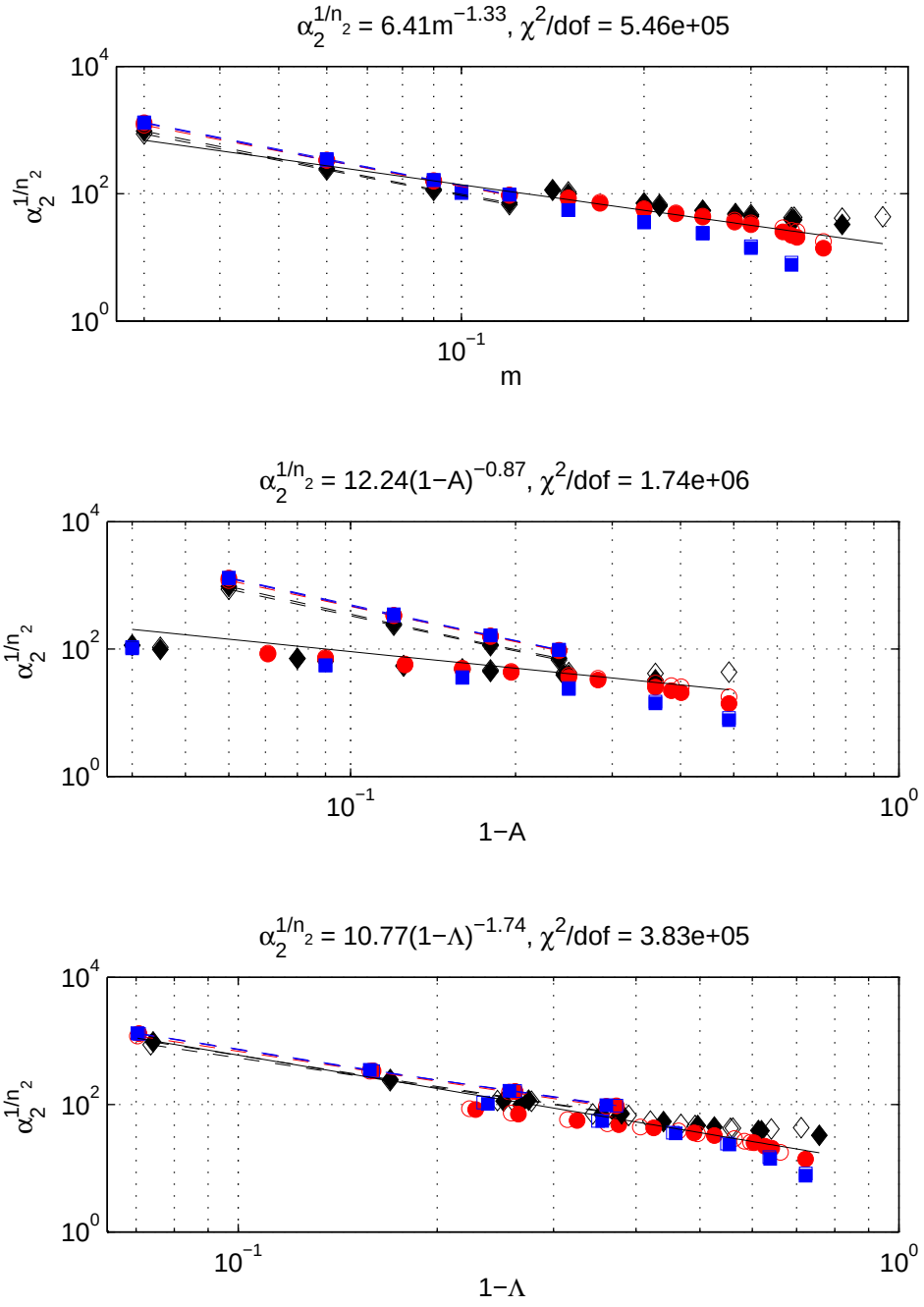

Figure D-1: Plot of α_2 versus various geometrical parameters.

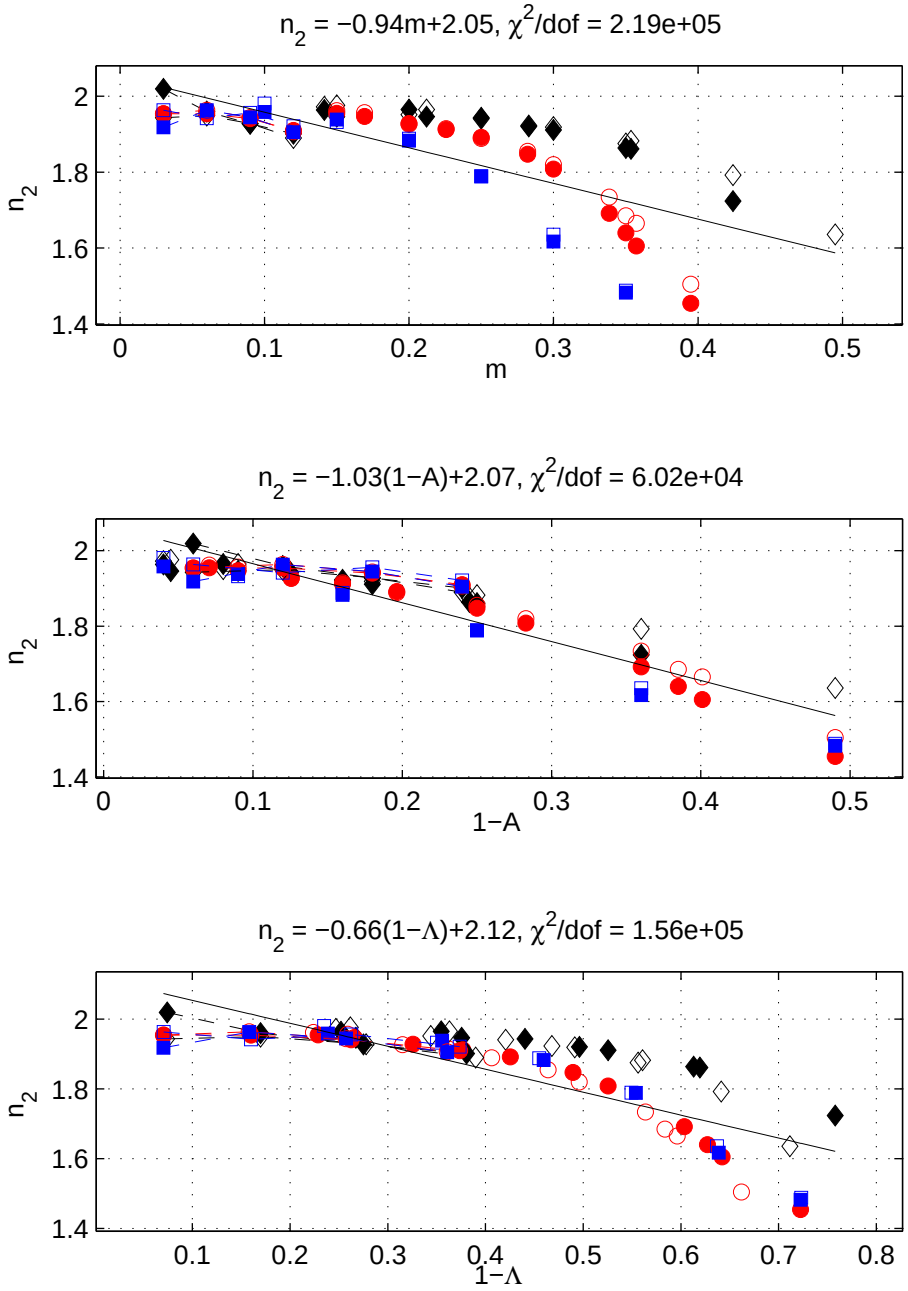

Figure D-2: Plot of n_2 versus various geometrical parameters.

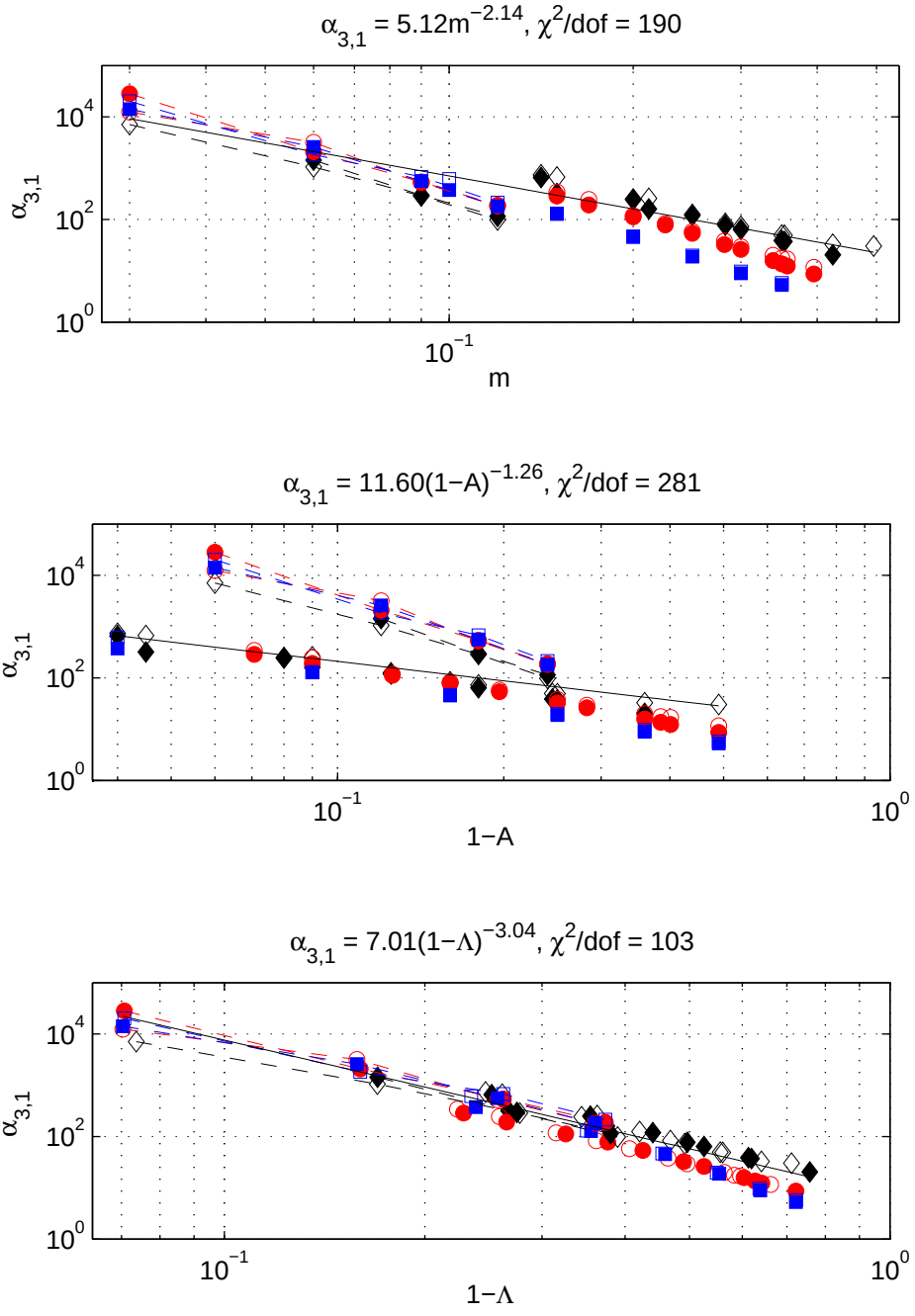

Figure D-3: Plot of $\alpha_{3,1}$ versus various geometrical parameters.

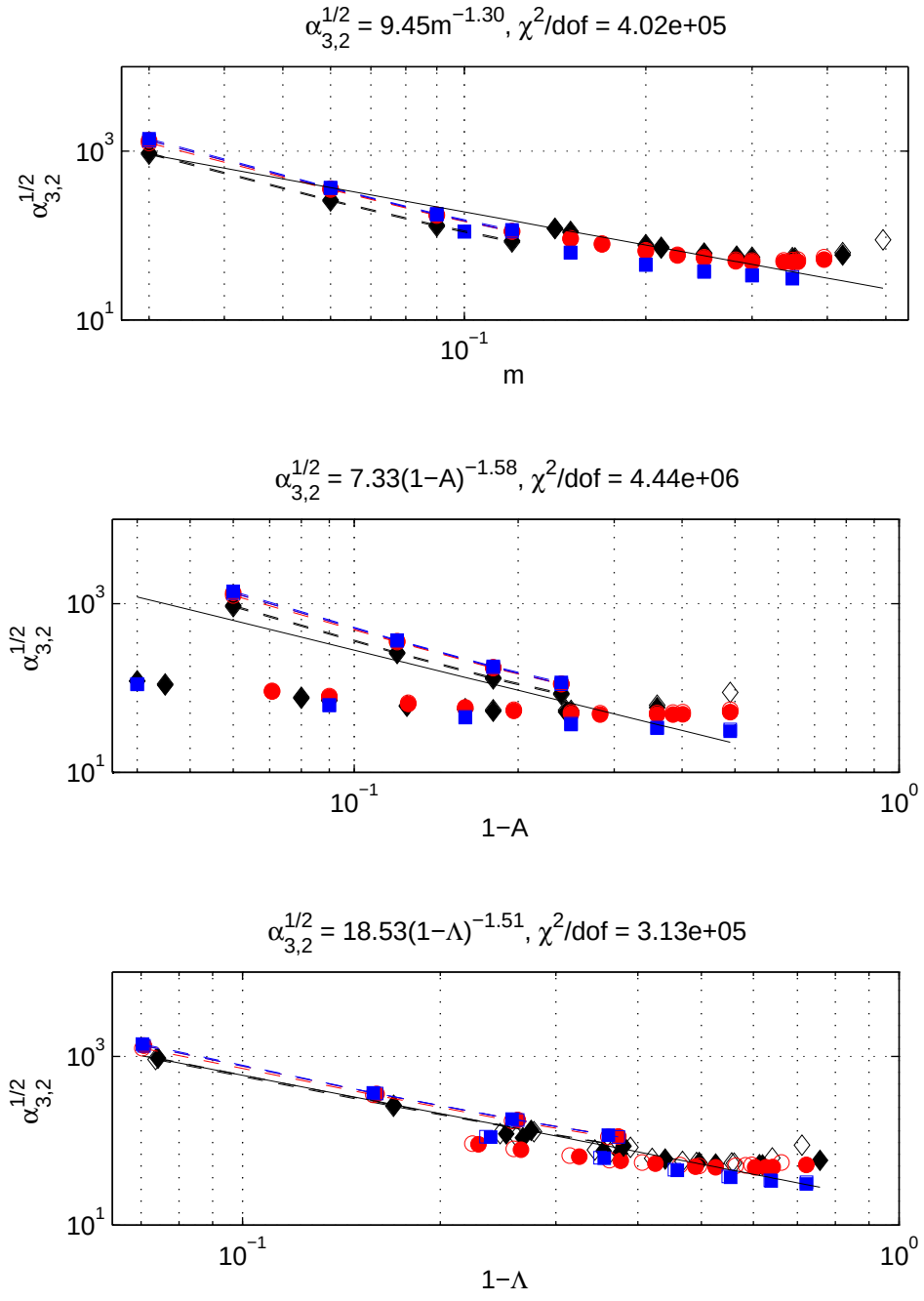

Figure D-4: Plot of $\alpha_{3,2}$ versus various geometrical parameters.

References

[1] A. Manz, N. Graber, and H.M. Widmer. Miniaturized total chemical analysis systems: a novel concept for chemical sensing. *Sensor. Actuat. B-Chem.*, 1(1-6):244–248, January 1990.

[2] Bing He, Niall Tait, and Fred Regnier. Fabrication of nanocolumns for liquid chromatography. *Anal. Chem.*, 70(18):3790–3797, August 1998.

[3] Daniel C. Harris. *Quantitative Chemical Analysis*. Freeman, 1999.

[4] C.L. Rice and R. Whitehead. Electrokinetic flow in a narrow cylindrical capillary. *J. Phys. Chem*, 69(11):4017–4024, 1965.

[5] E.B. Cummings, S.K. Griffiths, R.H. Nilson, and P.H. Paul. Conditions for similitude between the fluid velocity and electric field in electroosmotic flow. *Anal. Chem.*, 72(11):2526–2532, June 2000.

[6] J.G. Santiago. Electroosmotic flows in microchannels with finite inertial and pressure forces. *Anal. Chem.*, 73(10):2353–2365, May 2001.

[7] Christopher T. Culbertson, Stephen C. Jacobson, and J. Michael Ramsey. Dispersion sources for compact geometries on microchips. *Anal. Chem.*, 70(18):3781–3789, September 1998.

[8] Stewart K. Griffiths and Robert H. Nilson. Band spreading in two-dimensional microchannel turns for electrokinetic species transport. *Anal. Chem.*, 72(21):5473–5482, November 2000.

[9] Stewart K. Griffiths and Robert H. Nilson. Low-dispersion turns and junctions for microchannel systems. *Anal. Chem.*, 73(2):272–278, January 2001.

[10] Debashis Dutta and David T. Leighton, Jr. A low dispersion geometry for microchip separation devices. *Anal. Chem.*, 74(5):1007–1016, March 2002.

[11] Geoffrey Taylor. Dispersion of soluble matter in solvent flowing slowly through a tube. *Proc. R. Soc. Lon. Ser.-A*, 219(1137):186–203, August 1953.

[12] Geoffrey Taylor. Conditions under which dispersion of a solute in a stream of solvent can be used to measure molecular diffusion. *Proc. R. Soc. Lon. Ser.-A*, 225(1163):473–477, September 1954.

[13] R. Aris. On the dispersion of a solute in a fluid flowing through a tube. *Proc. R. Soc. Lon. Ser.-A*, 235(1200):67–77, April 1956.

[14] R.A. Wooding. Instability of a viscous liquid of variable density in a vortical Hele-Shaw cell. *J. Fluid Mech.*, 7(4):501–515, 1960.

[15] A. Bournia, J. Coull, and G. Houghton. Dispersion of gases in laminar flow through a circular tube. *Proc. R. Soc. Lon. Ser.-A*, 261(1305):227–236, April 1961.

[16] H.R. Bailey and W.B. Gogarty. Numerical and experimental results on the dispersion of a solute in a fluid in laminar flow through a tube. *Proc. R. Soc. Lon. Ser.-A*, 269(1338):352–367, September 1962.

[17] M.J. Lighthill. Initial development of diffusion in Poiseuille flow. *J. Inst. Maths. Applics.*, 2:97–108, 1966.

[18] Marco Latini and Andrew J. Bernoff. Transient anomalous diffusion in Poiseuille flow. *J. Fluid Mech.*, 441:399–411, August 2001.

[19] J.J. Fried and M.A. Combarnous. *Advances in Hydroscience*, volume 7, chapter 3. Academic, New York, 1971.

[20] Pierre M. Adler. *Porous Media: Geometry and Transports*, chapter 4. Butterworth-Heinemann Series in Chemical Engineering. Butterworth-Heinemann, Stoneham, MA, 1992.

[21] H. Brenner. Dispersion resulting from flow through spatially periodic porous media. *Philos. T. Roy. Soc. A*, 297(1430):81–133, July 1980.

[22] D.A. Hoagland and R.K. Prud'Homme. Taylor-Aris dispersion arising from flow in a sinusoidal tube. *AlChE J.*, 31(2):236–244, February 1985.

[23] D.A. Edwards, M. Shapiro, H. Brenner, and M. Shapira. Dispersion of inert solutes in spatially periodic two-dimensional porous media. *Transport Porous Med.*, 6(4):337–358, August 1991.

[24] A. Eidsath, R.G. Carbonell, S. Whitaker, and L.R. Herrmann. Dispersion in pulsed systems – III: Comparison between theory and experiments for packed beds. *Chem. Eng. Sci.*, 38(11):1803–1816, 1983.

[25] Ronald F. Probstein. *Physicochemical Hydrodynamics*, chapter 4. Wiley, New York, second edition, 1994.

[26] M. Kaviany. *Principles of Heat Transfer in Porous Media*, chapter 4. Mechanical Engineering Series. Springer, New York, second edition, 1995.

[27] Peter Henrici. *Applied and Computational Complex Analysis*. John Wiley & Sons, 1974.

[28] Roland W. Jeppson. Inverse formulation and finite difference solution for flow from a circular orifice. *J. Fluid Mech.*, 40(1):215–223, 1970.

[29] A. Thom and C.J. Apelt. *Field Computation in Engineering & Physics*. D. Van Nostrand, London, 1961.

[30] Albert Einstein. *Investigations on the Theory of the Brownian Movement*. Dover, New York, 1956.

[31] J.M. Floryan. Conformal-mapping-based coordinate generation method for channel flows. *J. Comput. Phys.*, 58(2):229–245, 1985.

[32] J.M. Floryan and Charles Zemach. Schwarz-Christoffel methods for conformal mapping of regions with a periodic boundary. *J. Comput. Appl. Math.*, 46(1-2):77–102, June 1993.

[33] K.W. Morton and D.F. Mayers. *Numerical Solution of Partial Differential Equations*. Cambridge University, 1994.

[34] Philippe G. Ciarlet. *Introduction to Numerical Linear Algebra and Optimisation*, volume 2 of *Cambridge texts in applied mathematics*. Cambridge University, 1989.

[35] G.K. Batchelor. *An Introduction to Fluid Dynamics*. Cambridge University, 2000.

[36] Louis H. Howell and Lloyd N. Trefethen. A modified Schwarz-Christoffel transformation for elongated regions. *SIAM J. Sci. Stat. Comp.*, 11(5):928–949, September 1990.

[37] Tobin A. Driscoll. Algorithm 756: A MATLAB toolbox for Schwarz-Christoffel mapping. *ACM T. Math. Software*, 22(2):168–186, June 1996.

[38] Tobin A. Driscoll and Lloyd N. Trefethen. *Schwarz-Christoffel Mapping*. Cambridge University, 2002.

[39] Tobin A. Driscoll. Schwarz-Christoffel Toolbox for MATLAB. `http://www.math.udel.edu/~driscoll/software/SC/`., 2003.

[40] Ahmed F. Ghoniem and Frederick S. Sherman. Grid-free simulation of diffusion using random walk methods. *J. Comput. Phys.*, 61(1):1–37, October 1985.

[41] Arthur S. Sherman and Charles S. Peskin. A monte carlo method for scalar reaction diffusion equations. *SIAM J. Sci. Stat. Comp.*, 7(4):1360–1372, October 1986.

[42] Elaine S. Oran and Jay P. Boris. *Numerical Simulation of Reactive Flow*. Elsevier, New York, 1987.

[43] Aaron L. Fogelson. Particle-method solution of two-dimensional convection-diffusion equations. *J. Comput. Phys.*, 100(1):1–16, May 1992.

[44] Alexandre Joel Chorin. Numerical study of slightly viscous flow. *J. Fluid Mech.*, 57(4):785–796, 1973.

[45] Joseph F. Lingevitch and Andrew J. Bernoff. Advection of a passive scalar by a vortex couple in the small-diffusion limit. *J. Fluid Mech.*, 270:219–249, July 1994.

[46] G.E.P. Box and Mervin E. Muller. A note on the generation of random normal deviates. *Ann. Math. Stat.*, 29(2):610–611, June 1958.

[47] Stephen Roberts. Accuracy of the random vortex method for a problem with non-smooth initial conditions. *J. Comput. Phys.*, 58(1):29–43, 1985.

[48] Philip R. Bevington and D. Keith Robinson. *Data Reduction and Error Analysis for the Physical Sciences*. McGraw-Hill, second edition, 1992.

[49] William H. Press, Brian P. Flannery, Saul A. Teukolsky, and William T. Vetterling. *Numerical Recipes in C: The Art of Scientific Computing*. Cambridge University, second edition, 1993.

[50] H.T. Lau. *A Numerical Library in C for Scientists and Engineers*. CRC, 1994.

[51] The MathWorks, Inc. Matlab v6.0.0.88 release 12. `http://mathworks.com/`., 2000.

[52] J.M. Hammersley and D.C. Handscomb. *Monte Carlo Methods*. Methuen, London, 1964.

[53] David Linton Johnson, Joel Koplik, and Lawrence M. Schwarz. New pore-size parameter characterizing transport in porous media. *Phys. Rev. Lett.*, 57(20):2564–2567, November 1986.

[54] David Linton Johnson, Joel Koplik, and Roger Dashen. Theory of dynamic permeability and tortuosity in fluid-saturaged porous media. *J. Fluid Mech.*, 176:379–402, 1987.

[55] M.T. Blom, E.F. Hasselbrink, H. Wensink, and A. van den Berg. Solute dispersion by electroosmotic flow in nonuniform microfluidic channels. In J. Michael Ramsey and Albert van den Berg, editors, *Micro Total Analysis Systems 2001*, pages 615–616, Monterey, CA, October 2001. Kluwer.